Landry, D., Bonamente, M., Giles, P., Maughan, B., & Joy, M. (2012). Chandra Measurements of a Complete Sample of X-ray Luminous Galaxy Clusters: the Gas Mass Fraction. *Monthly Notices of the Royal Astronomical Society*, *433*. https://doi.org/10.1093/mnras/stt901

This is an electronic version of an article published in MNRAS (August 21, 2013) 433 (4): 2790-2811.

Mon. Not. R. Astron. Soc. **000**, 1–20 (2012) Printed 21 November 2012 (MN LATEX style file v2.2)

arXiv:1211.4626v1 [astro-ph.CO] 19 Nov 2012

Chandra Measurements of a Complete Sample of X-ray Luminous Galaxy Clusters: the Gas Mass Fraction

D. Landry[1⋆], M. Bonamente[1,2], P. Giles[3], B. Maughan[3], and M. Joy[2]
[1] *Physics Department, University of Alabama in Huntsville, Huntsville, AL, USA 35899*
[2] *NASA National Space Science and Technology Center, Huntsville, AL, USA 35805*
[3] *HH Wills Physical Laboratory, University of Bristol, Bristol, UK*

Accepted . Received ; in original form

ABSTRACT

We present *Chandra* X-ray measurements of the gas mass fraction out to r_{500} for a complete sample of the 35 most luminous clusters from the Brightest Cluster Sample and the Extended Brightest Cluster Sample at redshift $z = 0.15 - 0.30$. The sample includes relaxed and unrelaxed clusters, and the data were analysed independently using two pipelines and two different models for the gas density and temperature. We measure an average of $f_{\rm gas}(r_{500}) = 0.163 \pm 0.032$, which is in agreement with the cosmic baryon fraction ($\Omega_{\rm b}/\Omega_{\rm M} = 0.167 \pm 0.006$) at the 1σ level, after adding the stellar baryon fraction. Earlier studies reported gas mass fractions significantly lower than the cosmic baryon fraction at r_{500}, and in some cases higher values that are consistent with the cosmic baryon fraction towards the virial radius. In this paper we show that the most X-ray luminous clusters in the redshift range $z = 0.15 - 0.30$ have a gas mass fraction that is consistent with the cosmic value at r_{500}.

1 INTRODUCTION

Clusters of galaxies are the largest known bound systems in the Universe and are formed from the collapse of primordial density fluctuations (Press & Schechter 1974; White & Rees 1978). The intracluster medium (ICM) is in the form of a hot ionized gas at $\sim 10^8$ K, and it contains most of the baryons in clusters. The remaining baryons are in stars and intracluster light, and account for a few percent of the total mass (Lin et al. 2003; Gonzalez et al. 2007; Giodini et al. 2009). The total cluster baryon fraction is therefore a combination of the baryons in stars and ICM, i.e., $f_{\rm b} = f_{\rm stars} + f_{\rm gas}$. Since clusters are extremely large and massive, baryons and dark matter originated from approximately the same comoving volume, and thus it is believed that their ratio should be representative of the Universe (e.g., Metzler & Evrard 1994). A number of studies have used the baryonic mass fraction to measure $\Omega_{\rm M}$ and found evidence for a low density Universe (Fabian 1991; White & Frenk 1991; White et al. 1993; Briel et al. 1992; David et al. 1995; White & Fabian 1995; Evrard 1997; Pen 1997; Ettori & Fabian 1999; Mohr et al. 1999; Grego et al. 2001; Allen et al. 2002, 2004; LaRoque et al. 2006; Allen et al. 2008; Ettori et al. 2009). Measuring the evolution of the gas mass fraction over a large redshift range, $f_{\rm gas}(z)$, allows cosmological quantities to be constrained (for recent reviews see Allen et al. 2008; Ettori et al. 2009 and references therein).

Current studies indicate that the cluster baryon fraction is typically lower than the cosmic baryon fraction as measured by the $\Omega_{\rm b}/\Omega_{\rm M}$ parameter (Vikhlinin et al. 2006; Afshordi et al. 2007; Arnaud et al. 2007; Giodini et al. 2009; Sun et al. 2009; Umetsu et al. 2009; Rasheed et al. 2010; Komatsu et al. 2011). This observation has raised questions on the whereabouts of these *missing baryons* (Rasheed et al. 2010). A possible explanation is that Active Galactic Nuclei (AGN) feedback may push the ICM towards the cluster outskirts (Metzler & Evrard 1994; Takizawa & Mineshige 1998; Bialek et al. 2001; Valdarnini 2003; McCarthy et al. 2007; Cavaliere & Lapi 2008; Bode et al. 2009).

To address this issue we measured the gas mass fraction for a complete sample of massive clusters at $z = 0.15 - 0.30$ from the *Brightest Cluster Sample* and its extension (Ebeling et al. 1998, 2000; Dahle 2006). The background of the surface brightness and temperature profiles limits the radius out to which masses can be measured accurately. Therefore we chose to limit our measurements for the entire sample to r_{500}, the radius within which the mass density is 500 times the critical density of the universe at the cluster's redshift. In cases of long exposures and high quality data, it is possible to use *Chandra* to detect clusters beyond r_{500}. For example, in Bonamente et al. (2012) we report the detection of A1835, one of the clusters in this sample, out to the virial radius. We calculate the total cluster baryon fraction by adding the baryons from stars and galaxies, and find that the baryon content in these high-luminosity clusters is consistent with the cosmic ratio $\Omega_{\rm b}/\Omega_{\rm M}$ at r_{500}.

This paper is structured in the following way: Section 2 briefly describes the sample of clusters, Section 3 discusses the *Chandra* data reduction, and Section 4 reviews the modelling of the X-ray data. We present our results in Section 5, possible systematic effects in Section 6, a comparison with other studies in Section 7, and discussion and conclusions in Section 8. Throughout this paper we assume a cosmology based on WMAP7 results with $H_0 = 70.2$ km s^{-1} Mpc^{-1}, $\Omega_{\rm M} = 0.27$, and $\Omega_\Lambda = 0.73$ (Komatsu et al. 2011).

2 CLUSTER SAMPLE

The sample we chose for this analysis is composed of 35 clusters from the Dahle (2006) sample (Table 1), a 90% complete sample of clusters with X-ray luminosities in the $0.1 - 2.4$ keV band of $L_{\rm X,\,keV} \geqslant 6 \times 10^{44}$ erg s^{-1} (for a concordance ΛCDM universe with $h = 0.7$) from the Brightest Cluster Sample (BCS, Ebeling et al. 1998) and the Extended BCS (eBCS, Ebeling et al. 2000) in the $z = 0.15 - 0.30$ redshift range. These clusters are estimated to have masses of $M_{180} \geqslant 5 \times 10^{14}$ h^{-1} M$_\odot$, making them the most massive in the (e)BCS sample (Dahle 2006). All of the clusters from this sample have archival *Chandra* data available for our analysis. The majority of the clusters have been observed with the ACIS imaging array (ACIS-I), and 6 with the ACIS spectroscopic array (ACIS-S). With this sample of clusters, we aim to measure the gas mass fraction out to r_{500} using high S/N X-ray data from *Chandra*, and then calculate the total baryon fraction using the stellar fraction from Gonzalez et al. (2007) and Giodini et al. (2009).

3 *CHANDRA* OBSERVATIONS AND DATA REDUCTION

Data reduction was done using the Chandra Interactive Analysis of Observations (CIAO[1]) software version 4.2 and the Chandra Calibration Database (CALDB[2]) version 4.3.1. The data reduction and subsequent analysis was performed by two separate pipelines: one was developed by D. Landry and M. Bonamente, and makes use of a Markov chain Monte Carlo method of analysis (e.g., Bonamente et al. 2004, 2006), the other was developed by P. Giles and B. Maughan (additional details are provided in Giles et al. 2012). Results from the two analyses, including temperature profiles and mass measurements, were found to be in statistical agreement, thus providing confidence on the results provided in this paper and in others to follow using the same sample (e.g., Giles et al. 2012).

As part of the data reduction, corrections were made for afterglows, charge transfer inefficiency (CTI), bad pixels and solar flares. Afterglows are caused from cosmic rays building up charge on the CCD, bad pixels take into account hot pixels and afterglow events, and CTI is due to proton damage to the ACIS chips that reduces the energy resolution. The variability of solar activity can cause periods of high background which need to be filtered out. A common way of removing these periods of solar flares is to follow the lightcurve filtering method of Markevitch et al. (2003). Before the lightcurve can be created, point sources of high and variable emission need to be excluded. The lightcurve is then created over the energy range $0.3 - 12.0$ keV for ACIS-I observations and $2.5 - 6.0$ keV for ACIS-S observations on a selected region of the *Chandra* CCD's used as the local background. A sample lightcurve is shown in Figure 1. This lightcurve was filtered with an iterative algorithm (`deflare` command in CIAO) that removes time intervals outside the 3σ range of the mean. The solid line shows the mean count rate for the observation and the red boxes show the regions that were filtered out. Most observations were taken in VFAINT mode, and in this case we applied VFAINT cleaning to both the cluster and blank-sky observations.

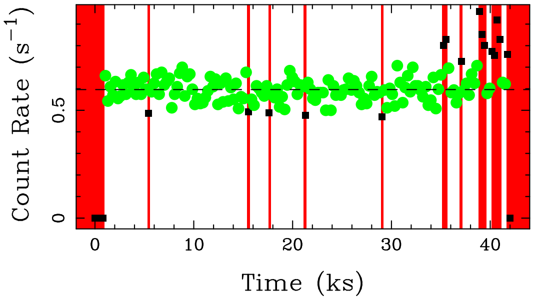

Figure 1. A sample lightcurve for observation 9371 of *Zwicky 3146*, showing excluded time intervals due to solar flares (red boxes). Lightcurves are created over the whole energy range, $0.3 - 12.0$ keV, using the local background region, $450 - 900''$ in this case. The mean count rate is 0.596 s^{-1} (dashed line) and the filtered exposure time is 36.3 ks.

Images were created in the $0.7 - 7.0$ keV band to measure the surface brightness as a function of radius. This energy band was chosen since in this energy range the effective area is highest and the background rate lowest. The most crucial aspect of the analysis of diffuse sources such as galaxy clusters is background subtraction. For this purpose, we use ACIS blank-sky composite event files and measurements of the local background taken from source-free regions of the cluster observation (Markevitch et al. 2003). Since all the clusters in the sample have redshifts in the $z = 0.15 - 0.30$ range, the emission does not extend across the entire detector, and we have a sufficiently large region to obtain a local background (see Figure 2). In nearly every cluster the local background was measured from an outer annulus beyond r_{200}, where the surface brightness was approximately constant, i.e., it has reached the background level. There are a few clusters that only have ACIS-S data available. For these clusters, the local background was taken from the adjacent ACIS-I chips. Point sources and extended substructures were detected and removed using `wavdetect` in CIAO and known sources were removed manually by visual inspection.

The local background of the cluster observation may differ from the ACIS blank-sky composites, since these observations were done at different times and positions in the sky, and the X-ray background has both spatial dependence (e.g., Snowden et al. 1997) and is time-variable (e.g., Takei et al. 2008). Although the background flux may vary with time, Hickox & Markevitch (2006) have shown that the ratio of the flux within the $2 - 7$ keV and $9.5 - 12$ keV bands is constant in time. We can therefore rescale the blank-sky spectrum by the ratio of the count rates in the $9.5 - 12$ keV band of cluster and blank-sky observations, and obtain a clean subtraction of the background in the spectral region of interest, which is $0.7 - 7.0$ keV (Hickox & Markevitch 2006). After subtracting the blank-sky background, resid-

---

[1] http://cxc.harvard.edu/ciao/
[2] http://cxc.harvard.edu/caldb/

Table 1. Cluster Sample

Cluster	z	D_A (Mpc)	N_H (10^{20} cm^{-2})	obsID	Exposure (ks)	Dynamical State
A115	0.1971	673.9	5.36	3233	43.6	Unrelaxed
A1423	0.2130	716.1	1.81	538	35.1	Unrelaxed
A1576	0.2790	876.1	1.08	7938	15.0	Unrelaxed
A1682	0.2260	749.5	1.04	11725	19.6	Unrelaxed
A1758	0.2790	876.1	1.03	7710	7.0	Unrelaxed
A1763	0.2230	741.9	0.82	3591	17.0	Unrelaxed
A1835	0.2532	816.3	2.04	6880 6881 7370	167.1	Relaxed
A1914	0.1712	601.8	1.06	3593 542	16.6	Unrelaxed
A2111	0.2290	757.1	1.84	11726 544	30.9	Unrelaxed
A2204	0.1520	545.5	5.67	7940	70.5	Relaxed
A2219	0.2256	748.5	1.76	896	41.5	Unrelaxed
A2261	0.2240	744.4	3.19	5007 550	22.5	Relaxed
A2390	0.2329	766.8	6.21	4193	19.7	Relaxed
A2552	0.3017	925.9	4.60	11730 3288	22.7	Unrelaxed
A2631	0.2780	873.8	3.55	11728 3248	25.0	Unrelaxed
A267	0.2310	762.1	2.75	1448	7.4	Unrelaxed
A520	0.1990	679.0	5.65	528 4215 9424 9426 9430	368.0	Unrelaxed
A586	0.1710	601.2	4.89	11723 530	15.8	Unrelaxed
A611	0.2880	896.1	4.46	3194	15.4	Relaxed
A665	0.1819	632.1	4.32	3586	14.3	Unrelaxed
A68	0.2546	819.7	4.96	3250	9.2	Unrelaxed
A697	0.2820	882.8	2.93	4217	15.4	Unrelaxed
A773	0.2170	726.5	1.28	3588 5006 533	37.3	Unrelaxed
A781	0.2987	919.4	1.65	534	9.9	Unrelaxed
A963	0.2060	697.7	1.25	903	23.0	Relaxed
MS 1455+2232	0.2578	827.2	3.18	4192 543	79.2	Relaxed
RX J0437.1+0043	0.2850	889.5	5.50	11729 7900	41.7	Relaxed
RX J0439.0+0715	0.2300	759.6	9.18	1449 3583	23.7	Relaxed
RX J1720.1+2638	0.1640	581.0	3.36	3224 4361	41.7	Relaxed
RX J2129.6+0005	0.2350	772.1	3.63	552 9370	35.9	Relaxed
Z2089	0.2347	771.3	2.86	10463 7897	39.4	Relaxed
Z3146	0.2906	901.8	2.46	909 9371	81.3	Relaxed
Z5247	0.2300	759.6	1.61	11727 539	19.2	Unrelaxed
Z5768	0.2660	846.4	1.49	7898	10.4	Unrelaxed
Z7215	0.2897	899.9	1.40	7899	13.0	Unrelaxed

uals may still be present in the soft $0.7-2$ keV band. These soft residuals may be due to Galactic and extragalactic emission, as well as residual solar flares that were not removed by lightcurve filtering (e.g., Snowden et al. 1997). When present, the soft residual spectrum is then fit with a power law and a plasma emission model, and this model of the soft residuals is taken into account in the cluster spectra (as done in, e.g., Bulbul et al. 2010; Hasler et al. 2012). Figure 3 shows an example of soft residuals below 2 keV for observation 6880 of *Abell 1835*. Multiple observations were reduced individually to apply the correct calibration to each dataset. The cluster surface brightness profile is obtained from merged images, and the temperature profile from fitting spectra from different observations simultaneously.

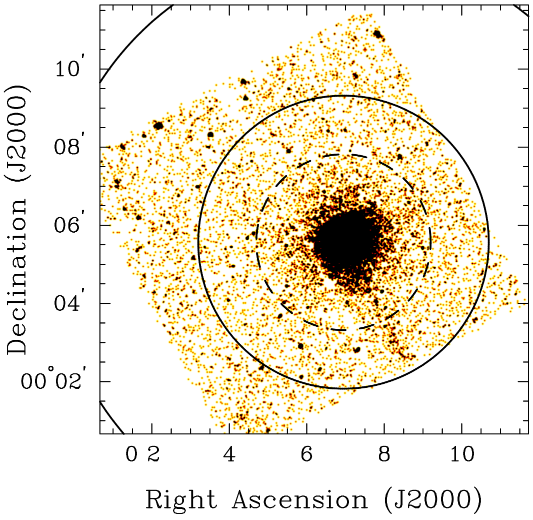

Figure 2. The local background region used for ACIS-I observation 9371 of *Zwicky 3146*. The annulus used for the local background is from $450-900''$ (solid lines). The dashed line indicates r_{500} and is approximately $270''$.

4 MODELLING AND ANALYSIS OF THE *CHANDRA* DATA

The total mass of a cluster can be inferred from the density and temperature of the X-ray emitting ionized plasma, assuming that the hot gas is in hydrostatic equilibrium with the gravitational cluster potential. Thus, we can write the

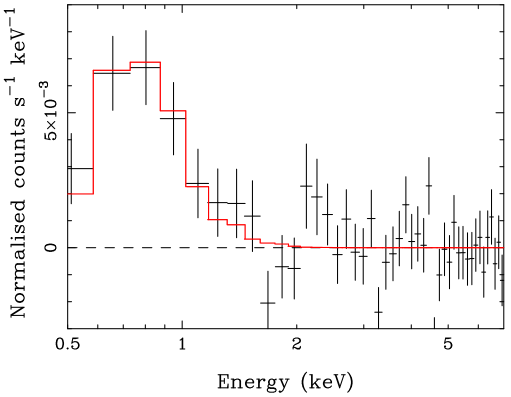

Figure 3. Spectrum of the local background (beyond $\sim 750''$) for observation 6880 of *Abell 1835*. This shows the soft residuals (below 2 keV) fit with an unabsorbed thermal plasma model with $kT \sim 0.25$ keV.

total mass as

$$M_{\rm tot}(r) = \frac{-k_{\rm B} T(r)\, r}{\mu m_{\rm p} G} \left(\frac{d \ln n_{\rm e}(r)}{d \ln r} + \frac{d \ln T(r)}{d \ln r} \right), \qquad (1)$$

where $k_{\rm B}$ is the Boltzmann constant, $T(r)$ is the temperature profile, μ is the mean molecular weight, $m_{\rm p}$ is the mass of a proton, G is the gravitational constant, and $n_{\rm e}(r)$ is the number density of electrons. The mass of the hot gas is calculated as

$$M_{\rm gas}(r) = 4\pi \mu_{\rm e} m_{\rm p} \int n_{\rm e}(r)\, r^2\, dr, \qquad (2)$$

where $\mu_{\rm e}$ is the mean molecular weight of the electrons. We use high resolution X-ray imaging and spectroscopy from the *Chandra* X-ray Observatory to determine $n_{\rm e}(r)$ and $T(r)$. Specifically, the observed X-ray surface brightness is related to the electron number density by the following equation

$$S_{\rm X} = \frac{1}{4\pi(1+z)^3} \int n_{\rm e}^2(r) \Lambda_{\rm ee}(T_{\rm e})\, dl \qquad (3)$$

where z is the redshift, $\Lambda_{\rm ee}(T_{\rm e})$ is the plasma emissivity (counts cm^3 s^{-1}) and the integral is along the line of sight through the cluster. The linear distance r in these equations is given by $r = \theta D_{\rm A}$, where θ is the apparent angular size and $D_{\rm A}$ is the angular diameter (Carroll et al. 1992). To measure the density from the surface brightness, the angular diameter must be known. The value of $D_{\rm A}$ can be calculated from the following equation (valid for $\Omega_k = 0$):

$$D_{\rm A} = \frac{c}{(1+z)H_0} \int_0^z \frac{1}{E(z)}\, dz,$$

where $E^2(z) = \Omega_{\rm M}(1+z)^3 + \Omega_\Lambda$ and H_0 is the Hubble constant. The temperature profile is determined from radially-averaged X-ray spectra fit to an APEC optically-thin emission model (Smith et al. 2001), with Galactic H I column density measured from the Leiden-Argentine-Bonn survey (Kalberla et al. 2005). We used the XSPEC software version 12.6.0s (Arnaud 1996).

We use the Vikhlinin et al. (2006) model that describes the density and temperature of the cluster to fit the *Chandra* data. The three-dimensional gas density is modelled as a generalisation of the β-model,

$$n_{\rm p} n_{\rm e} = n_0^2 \frac{(r/r_{\rm c})^{-\alpha}}{(1+r^2/r_{\rm c}^2)^{3\beta-\alpha/2}} \frac{1}{(1+r^\gamma/r_{\rm s}^\gamma)^{\varepsilon/\gamma}} + \frac{n_{02}^2}{(1+r^2/r_{\rm c}^2)^{3\beta_2}} \qquad (4)$$

and uses a total of ten parameters. The model used for the temperature profile is given by the phenomenological function

$$T(r) = T_0 \frac{(r/r_{\rm cool})^{a_{\rm cool}} + (T_{\rm min}/T_0)}{(r/r_{\rm cool})^{a_{\rm cool}} + 1} \times \frac{(r/r_{\rm t})^{-a}}{[1+(r/r_{\rm t})^b]^{c/b}}, \qquad (5)$$

which has eight parameters and thus enough degrees of freedom to model nearly any smooth temperature distribution. The second term in the temperature profile describes the region outside of the cool-core as a broken power law with a transition region. Therefore, the Vikhlinin et al. (2006) model has a total of 18 parameters. In our analysis, we used the following constraints for all clusters: $n_{02} = 0$, $\alpha = 0$, $\gamma = 3$, and $\varepsilon < 5$. For certain clusters with lower S/N, we fixed additional parameters.

To assess biases from the use of a particular parameterization of the thermodynamic quantities, we also model all clusters with the Bulbul et al. (2010) model. This model gives analytic functions for temperature, density, and gas pressure, assuming a polytropic equation of state and hydrostatic equilibrium outside of the cluster core. Similar to the Vikhlinin et al. (2006) model, it accounts for cooling of the gas in the core, and the temperature profile is

$$T(r) = T_0 \left(\frac{1}{(\beta-2)} \frac{(1+r/r_{\rm s})^{\beta-2} - 1}{r/r_{\rm s}(1+r/r_{\rm s})^{\beta-2}} \right) \tau_{\rm cool}. \qquad (6)$$

The function

$$\tau_{\rm cool} = \frac{(r/r_{\rm cool})^{a_{\rm cool}} + \xi}{(r/r_{\rm cool})^{a_{\rm cool}} + 1} \qquad (7)$$

has been adopted from Vikhlinin et al. (2006). In Equation 7, the quantity $\xi = T_{\rm min}/T_0$ is a free parameter ($0 < \xi < 1$) that measures the amount of central cooling. With this temperature profile, the gas density profile can be determined from the polytropic equation of state,

$$n_{\rm e}(r) = n_{\rm e0} \left(\frac{1}{(\beta-2)} \frac{(1+r/r_{\rm s})^{\beta-2} - 1}{r/r_{\rm s}(1+r/r_{\rm s})^{\beta-2}} \right)^n \tau_{\rm cool}^{-1}, \qquad (8)$$

The Bulbul et al. (2010) model therefore has a total of 8 parameters. The comparison of results from the two models can be found in Section 6.

The emissivity for thermal bremsstrahlung emission at energy E is

$$\Lambda_{ee} \propto n^2 T^{-1/2} e^{-E/k_{\rm B}T},$$

where n is the number density and T is the temperature. The two X-ray observables, $S_{\rm X}$ and T, are therefore not completely independent. To determine the best-fit parameters of the models, we use a Markov chain Monte Carlo (MCMC) method with a Metropolis-Hastings selection algorithm described in Bonamente et al. (2004). Although both models have parameters that can be correlated to one another (e.g., Hasler et al. 2012), the MCMC method accounts for these correlations, and model parameters and all derivative quantities such as masses and the gas mass fraction can be computed accurately.

In the analysis of the surface brightness and temperature profile data we follow Bulbul et al. (2010) and Hasler et al. (2012) and add a 1% systematic uncertainty for each bin of the surface brightness and a 10% systematic uncertainty for each bin of the temperature data. In Section 6 we describe additional sources of systematic errors that can affect our measurements. Selected temperature fits for both the Vikhlinin et al. (2006) and Bulbul et al. (2010) model are shown in Figure 4 (see Appendix A for temperature profiles and fits for all clusters). To measure masses at r_{500}, we need to fit the data beyond this radius to constrain the slope of the temperature profile. Out of the entire sample of 35 clusters, 28 have temperature and surface brigthness measurements out to or beyond r_{500}, and only 7 required slight extrapolation out to r_{500} (see Appendix A for additional details).

5 MEASUREMENT OF THE GAS MASS FRACTION

5.1 Results for the Entire Sample

The gas mass, total mass, and gas mass fraction for each cluster are reported in Table 11. We calculated the median and 68.3% confidence interval for the average gas mass fraction from the combined chains of all clusters, to find

$$\begin{cases} f_{\rm gas}(r_{2500}) = 0.110 \pm 0.017 \\ f_{\rm gas}(r_{500}) = 0.163 \pm 0.032. \end{cases} \tag{9}$$

The average radial profile of the gas mass fraction for all clusters is shown in Figure 5 and shows an increase with radius as also found in previous studies, e.g., Vikhlinin et al. (2006) and Rasheed et al. (2010).

Since clusters are the largest gravitationally bound structures in the Universe, the baryon fraction should be representative of the cosmic ratio $\Omega_{\rm b}/\Omega_{\rm M}$. Current measurements from WMAP indicate that the cosmic baryonic fraction is

$$\Omega_{\rm b}/\Omega_{\rm M} = 0.167 \pm 0.006 \tag{10}$$

(Komatsu et al. 2011). To accurately compare the gas mass fraction with the cosmic baryon fraction, baryons in stars and galaxies need to be taken into account. Giodini et al. (2009) measured the baryon fraction of stars and galaxies and determined this stellar mass fraction as a function of M_{500}, finding

$$f_{\rm stars,\,500} = 0.019 \pm 0.002 \tag{11}$$

for clusters with mass $M(r_{500}) \simeq 7.1 \times 10^{14}$ M$_\odot$. This result is slightly higher than the value reported by Gonzalez et al. (2007), who measure $f_{\rm stars,\,500} \simeq 0.012$ for the same mass range. Including the Giodini et al. (2009) results in our measurements of the gas mass fraction, we estimate the baryon fraction $f_{\rm b}(r_{500})$ for our sample as

$$f_{\rm b}(r_{500}) = 0.182 \pm 0.032. \tag{12}$$

The difference between the average baryon fraction measured at r_{500} and the cosmic baryon fraction from WMAP is therefore

$$f_{\rm b}(r_{500}) - \Omega_{\rm b}/\Omega_{\rm M} = +0.015 \pm 0.033,$$

i.e., our measurements match the known cosmic baryon fraction at the 1σ level at r_{500}, as also shown in Figure 5. The measurement of the baryon fraction using the Bulbul et al. (2010) model also agrees with $\Omega_{\rm b}/\Omega_{\rm M}$ (see Section 6 for discussion).

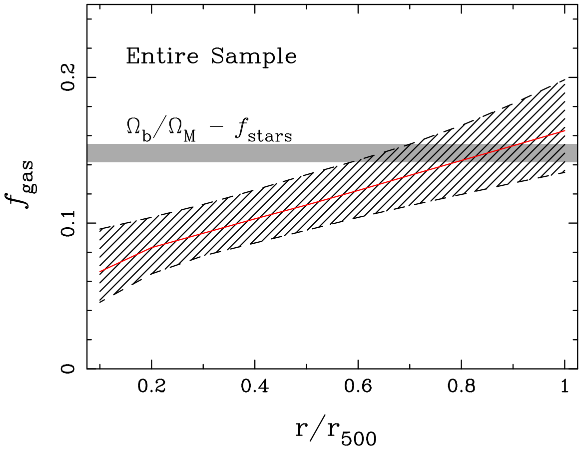

Figure 5. Average gas mass fraction profile for the Vikhlinin et al. (2006) model for all the clusters in the sample, with $f_{\rm gas}(r_{500}) = 0.163 \pm 0.032$. The red line is the median and the hatched region is the 68.3% confidence interval from the combined Monte Carlo Markov chains for all clusters. The grey envelope is the difference of the cosmic baryon fraction and the fraction of baryons in stars and galaxies. Using the results from Komatsu et al. (2011) and Giodini et al. (2009), we use the value of $\Omega_{\rm b}/\Omega_{\rm M} - f_{\rm stars} = 0.148 \pm 0.006$.

5.2 Results for Relaxed and Unrelaxed Clusters

We used three parameters to determine if a cluster can be classified as dynamically relaxed and host a cool-core: centroid shift for the dynamical state, central cooling time and cuspiness for the presence of a cool-core. For clusters with high quality data, the central cooling time is the best method for determining if it has a cool-core or not (Hudson et al. 2010). We calculated the central cooling time as

$$t_{\rm cool} \;=\; 8.5 \times 10^{10}\ {\rm yr} \left(\frac{n_{\rm p}}{10^{-3}\ {\rm cm}^{-3}}\right)^{-1} \left(\frac{T_{\rm g}}{10^8\ {\rm K}}\right)^{1/2}, \tag{13}$$

where $n_{\rm p}$ is the number density of protons and $T_{\rm g}$ is the central temperature of the gas (Sarazin 1988), using the best-fitting temperature profile at $r = 0.048\ r_{500}$ as the central temperature. Cuspiness is defined as the logarithmic derivative of the density profile,

$$\alpha \;=\; \frac{d\log n_{\rm e}}{d\log r}, \tag{14}$$

evaluated at $r = 0.04\,r_{500}$ (Vikhlinin et al. 2007). Hudson et al. (2010) indicate that, for low quality data, this parameter is a good indicator for the presence of a cool-core. The centroid shift is defined as the standard deviation of the distance between the peak X-ray emission and the centroid (Poole et al. 2006). We measured the centroid shifts in annular bins centered on the X-ray peak decreasing by

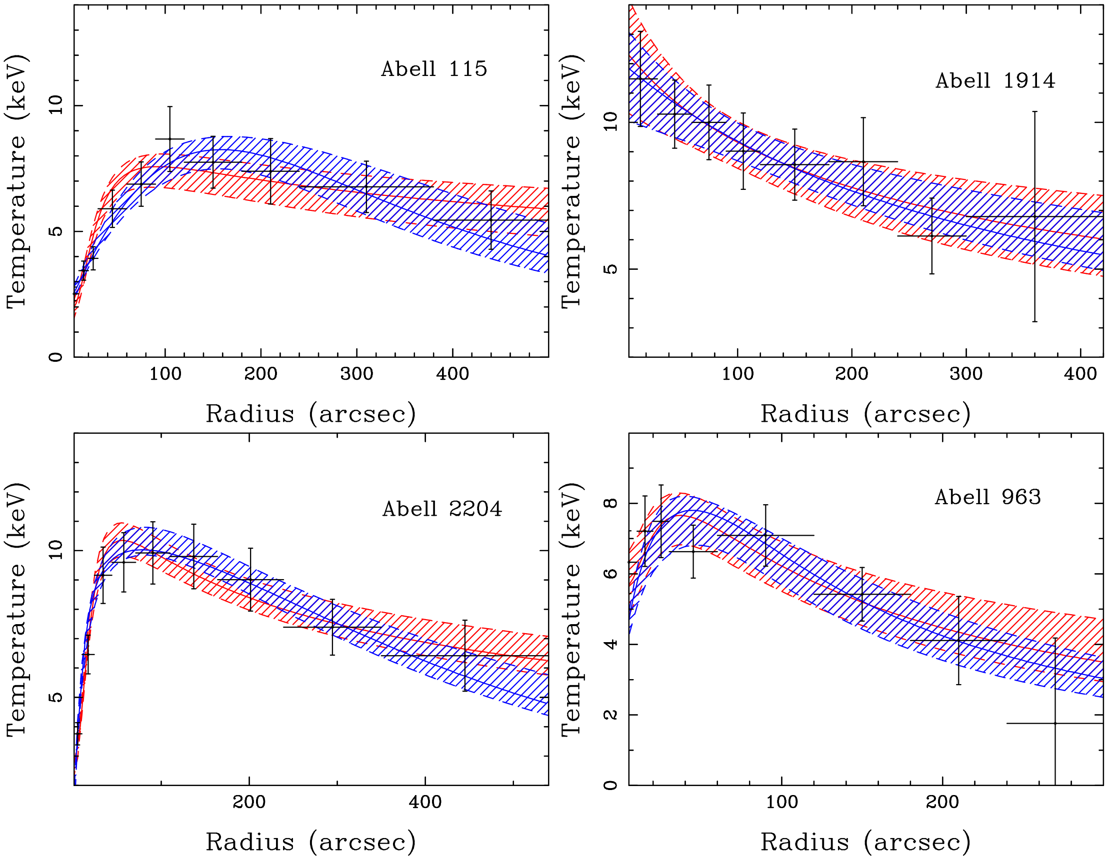

Figure 4. Temperature profiles for selected clusters using the Vikhlinin et al. (2006) model (blue) and the Bulbul et al. (2010) model (red). The solid lines show the best-fit values, and the hatched region is the 68.3% confidence interval.

$0.05\,r_{500}$, as suggested by Poole et al. (2006). We calculated the central cooling times, cuspiness, and centroid shifts for all the clusters in the sample, and we classified relaxed clusters as those which satisfied the following three conditions: (i) $\langle w \rangle < 0.009\,r_{500}$, (ii) $\alpha > 0.65$, and (iii) $t_{\rm cool} < 6.5$ Gyr (see Giles et al. 2012 for more details). This classification results in 13 relaxed clusters and 22 unrelaxed clusters, as shown in Table 1.

We calculated the gas mass fraction at r_{2500} and r_{500} for both subsamples of relaxed clusters and unrelaxed clusters (see Table 2). Our results show that at both radii the gas mass fractions for relaxed clusters are in excellent agreement with that of unrelaxed clusters, and that both sub-samples are statistically consistent with the cosmic baryon fraction at r_{500} (see Figure 6). The agreement of the gas mass fraction between relaxed and unrelaxed clusters may be an indication that hydrostatic mass estimates are reliable for unrelaxed clusters out to r_{500}. Giles et al. (2012) discusses further the reliability of hydrostatic mass estimates.

6 SYSTEMATICS AND PHYSICAL PROCESSES AFFECTING THE GAS MASS FRACTION

This section describes certain sources of systematic error and physical processes that may affect X-ray measurements of the gas mass fraction.

Table 2. Measurements of $f_{\rm gas}$ using the Vikhlinin et al. (2006) Model

Sample	$f_{\rm gas}$ r_{2500}	$f_{\rm gas}$ r_{500}
Relaxed	0.111 ± 0.017	0.155 ± 0.026
Unrelaxed	0.108 ± 0.017	0.173 ± 0.036
All Clusters	0.110 ± 0.017	0.163 ± 0.032

6.1 Assumption of hydrostatic equilibrium

One way in which the gas mass fraction can be affected is from the assumption of hydrostatic equilibrium. If there is an additional component of pressure that is non-thermal, then this must be taken into account when applying the equation of hydrostatic equilibrium. The hydrostatic equilibrium equation is used to determine the total mass of the cluster from X-ray observations,

$$M_{\rm tot}(r) = -\frac{r^2}{\rho G}\frac{dP}{dr}, \tag{15}$$

where ρ and P are the density and pressure, respectively, of the hot gas. Continued accretion of the gas onto clusters along filaments, mergers, and supersonic motions of galaxies through the intracluster medium are believed to cause gas motions which give rise to non-thermal pressure (Lau et al. 2009). Suppose that the pressure of the hot gas consists of a

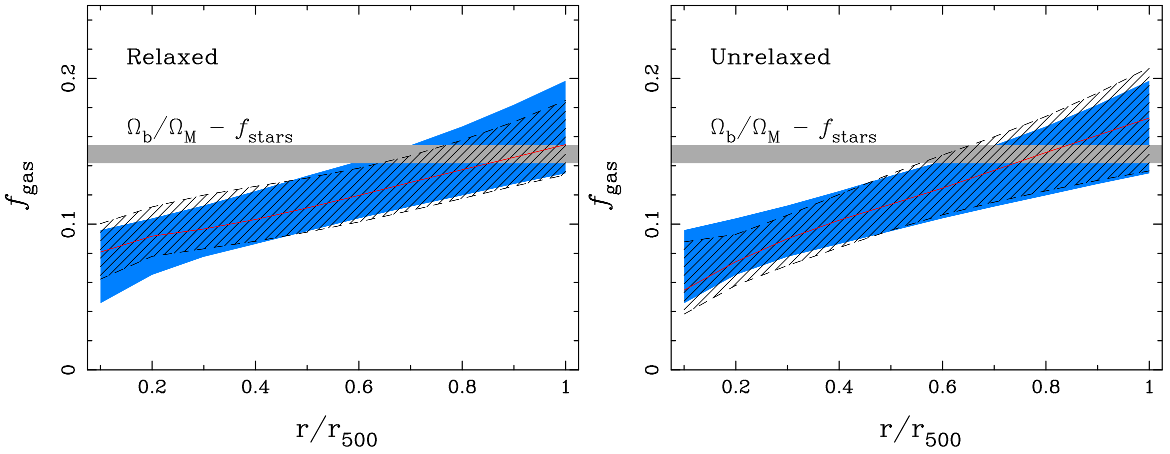

Figure 6. Left: Average gas mass fraction profile using the Vikhlinin et al. (2006) model for the relaxed clusters, with $f_{\rm gas}(r_{500}) = 0.155 \pm 0.026$. Right: Average gas mass fraction profile for the unrelaxed clusters, with $f_{\rm gas}(r_{500}) = 0.173 \pm 0.036$. The red line is the median and the hatched region is the 68.3% confidence interval. The blue region is the average $f_{\rm gas}$ profile for all clusters. The grey envelope is the difference of the cosmic baryon fraction and the fraction of baryons in stars and galaxies, $\Omega_{\rm b}/\Omega_{\rm M} - f_{\rm stars} = 0.148 \pm 0.006$ (Giodini et al. 2009; Komatsu et al. 2011).

thermal and a non-thermal component, $P = P_{\rm th} + P_{\rm non\text{-}th}$. Then, the equation for total mass becomes

$$M_{\rm tot}(r) = -\frac{r^2}{\rho G}\left(\frac{dP_{\rm th}}{dr} + \frac{dP_{\rm non\text{-}th}}{dr}\right), \tag{16}$$

and yields a higher mass compared to the mass from thermal pressure only. Separating the mass into components which correspond to different pressure terms, the total mass can be written as

$$M_{\rm tot} = M_{\rm th} + M_{\rm non\text{-}th}. \tag{17}$$

Lau et al. (2009) shows that the hydrostatic mass underestimates the true mass for several simulated clusters, especially at large radii. Gas motions are expected to cause a non-thermal pressure in the amount of $\gtrsim 5\% - 15\%$ of the thermal pressure, and this non-thermal pressure will cause an underestimate of mass at large radii of $8\% \pm 2\%$ for relaxed systems and $11\% \pm 6\%$ for unrelaxed systems at r_{500} (Lau et al. 2009). In the presence of non-thermal pressure the true mass of the cluster is given by Equation 16, and the use of Equation 15 leads to an underestimate of the mass, and therefore an *overestimate* of the gas mass fraction. Giles et al. (2012) compared X-ray hydrostatic masses with weak-lensing masses for these clusters and found that the total mass obtained through X-ray measurements is underestimated by a factor of 1.21 ± 0.23 and 1.41 ± 0.15 for relaxed and unrelaxed clusters, respectively. This comparison would indicate a departure from hydrostatic equilibrium that causes the gas mass fraction to be overestimated. Based on the Lau et al. (2009) results, we assess a systematic uncertainty of $+10\%$ on $M_{\rm tot}(r_{500})$ for all clusters. This results in a possible systematic error of -10% on $f_{\rm gas}(r_{500})$.

6.2 Uncertainties in the calibration of the Chandra data

Uncertainties in the calibration of the *Chandra* X-ray data can also affect the measurement of the gas mass fraction. The efficiency of the ACIS detector has a spatial dependency, and deviates from being uniform at the ±1% level (Bulbul et al. 2010). Therefore, we added a ±1% uncertainty to each data point in the surface brightness data prior to the analysis.

The temperature profile used in the analysis is also subject to various sources of systematic uncertainty. One source of uncertainty is from the subtraction of the local background. To subtract the background, we first have to rescale the blank-sky spectrum to match that of the high-energy ($9.5 - 12$ keV) flux of the cluster observation, as described in Section 3. We estimated the effect of the background subtraction using the longest observation of *Abell 1835* (ObsID 6880) which has the highest S/N. To obtain a clean background subtraction, we found that the fractional correction to the blank-sky spectrum is -0.04 ± 0.01. We measured the temperature in an outer region out to $\sim r_{500}$ (radii $240 - 330''$) using the best-fit correction factor (-0.04) and obtained $kT = 5.77$ keV. We then changed the correction to the blank-sky spectrum to -0.03 and -0.05 to over- and under-subtract the background by $\pm 1\sigma$. With these values, we found the temperature changed to $kT = 5.38$ keV and 6.23 keV, respectively. Therefore, we concluded that the uncertainty in temperature due to the background subtraction is approximately ±7.5%. Another source of error is caused by contamination on the Optical Blocking Filter, which is known to affect cluster temperatures by up to 5% (Bulbul et al. 2010; Hasler et al. 2012). Adding these errors in quadrature, we use a ±10% systematic uncertainty in fitting the temperature data. This additional error was therefore added to each temperature datapoint prior to the analysis.

6.3 Uncertainties due to asphericity of the cluster emission

To measure cluster masses, we assume spherical symmetry even though many clusters have a disturbed morphology. To estimate the uncertainty due to spherical symmetry we considered one of the most disturbed clusters, *Abell 520.* We used observation ID 9426 since this observation had the

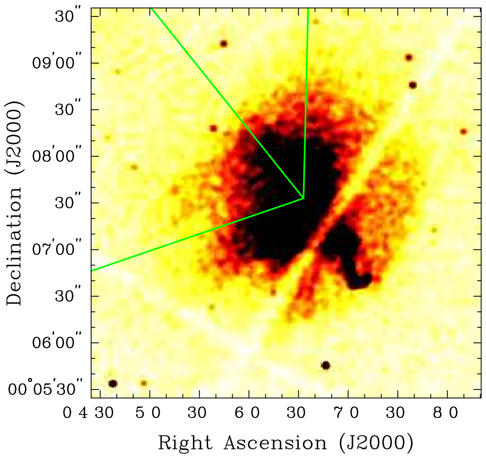

Figure 7. Image of *Abell 520* showing the two sections analysed. The regions were selected by using the temperature map from Govoni et al. (2004).

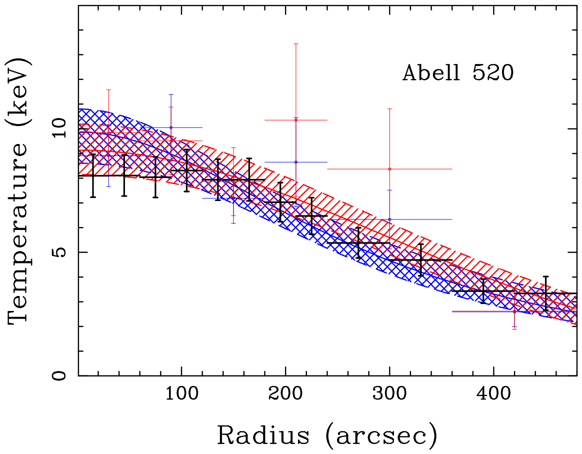

Figure 8. Temperature profiles for the two sections analysed from Figure 7. The blue lines correspond to the eastern section and red corresponds to the northern section. The black data is the temperature profile obtained from analysing the whole cluster.

best aimpoint for our task. After performing the *Chandra* data reduction as described in Section 3, this observation was left with 96.5 ks of filtered exposure time. Using the 2-D temperature map of *Abell 520* from Govoni et al. (2004), we studied two sections of the cluster (see Figure 7): the northern section (with respect to the azimuthal angle) was chosen because it encompasses a gas with temperature $\sim$ 10 keV, while the eastern section was selected because of its cooler temperature of $\lesssim 8$ keV(Govoni et al. 2004). The two sections are representative of an extreme case of disturbed dynamical state that causes azimuthal differences in temperature and surface brightness. We extracted a temperature profile and surface brightness profile for the two sectors, and measured masses using only the data within these azimuthal angles. Figure 8 shows the temperature fits to the two sections. For the northern section, we calculated $f_{\rm gas}(r_{2500}) = 0.109 \pm 0.010$ and $f_{\rm gas}(r_{500}) = 0.179 \pm 0.015$; for the eastern section, $f_{\rm gas}(r_{2500}) = 0.101 \pm 0.007$ and $f_{\rm gas}(r_{500}) = 0.202 \pm 0.015$ (see Table 3 for more information). Using these measurements we estimate that there is a $\pm 6\%$ and $\pm 8\%$ systematic uncertainty in the gas mass fraction due to the assumption of spherical symmetry at r_{2500} and r_{500}, respectively.

6.4 Effects of model parameterization

Another source of error is due to the choice of model for the X-ray data. In addition to the baseline model by Vikhlinin et al. (2006), we repeated all measurements of the gas mass fraction with the Bulbul et al. (2010) model (see Section 4 for more detail about the models). Model parameters for both fits are reported in Tables 8, 9, and 10 (fixed parameters are shown without error bars), and the mass measurements using both models can be found in Table 11. A plot of the average gas mass fraction profile for the entire sample using the Bulbul et al. (2010) model is given in Figure 9, showing an excellent agreement at all radii with the Vikhlinin et al. (2006) model results.

We also compare the average values of r_Δ, $M_{\rm gas}$, $M_{\rm tot}$, and $f_{\rm gas}$ for the two models in Table 4; plots comparing each measurement can be found in Figure 10. By using these two different models to measure cluster masses we conclude there is a $6\% \pm 2\%$ uncertainty on $f_{\rm gas}$ at r_{2500} and a $1\% \pm 2\%$ uncertainty on $f_{\rm gas}$ at r_{500} due to modelling the data, i.e., the two models give the same answer at large radii.

We also used two independent pipelines to reduce and analyse the same *Chandra* data and measure masses, one developed by Landry and Bonamente (LB) and one by Giles and Maughan (GM). The two analyses resulted in the following differences in the measurement of the gas mass fraction:

$$\begin{cases} f_{\rm gas}(r_{2500}): \dfrac{\rm GM - LB}{\rm GM} = -2\% \pm 3\% \\ f_{\rm gas}(r_{500}): \dfrac{\rm GM - LB}{\rm GM} = -3\% \pm 3\%. \end{cases}$$

This result indicates that our measurements of the gas mass fraction using the two pipelines are consistent with one another. We therefore believe that our measurements of the gas mass fraction are robust to the various choices made during the analysis.

We note that a recent study by Mantz & Allen (2011) shows how parametric models for the density and temperature of the ICM introduce an implicit prior due to the assumption of hydrostatic equilibrium. If the models are not flexible enough or too general, then the derived scaling relations will be biased towards self-similarity (Mantz & Allen 2011).

6.5 Uncertainties due to clumping of the gas

Clumping of the gas will also affect the gas mass fraction. The main process for X-ray emission in clusters is through bremsstrahlung emission, which is proportional to $n_{\rm e}^2$. If the gas is clumped, instead of being distributed uniformly, then the density of electrons $n_{\rm e}$ will be overestimated by making the assumption of a uniform distribution. Observations and simulations show that gas clumping may be most evident in the outskirts of clusters ($r > r_{500}$, Mathiesen et al. 1999; Nagai & Lau 2011; Eckert et al. 2012), though even within r_{500} the gas mass can be overestimated by $\sim$ 10% due to clumping (Mathiesen et al. 1999). Therefore, our measurements of $f_{\rm gas}$ at r_{500} would remain consistent with the cos-

Table 3. Cluster Properties of Sections of *Abell 520*

Cluster	$\Delta = 2500$				$\Delta = 500$			
	r_Δ (arcsec)	$M_{\rm gas}$ (10^{13} M$_\odot$)	$M_{\rm tot}$ (10^{14} M$_\odot$)	$f_{\rm gas}$	r_Δ (arcsec)	$M_{\rm gas}$ (10^{13} M$_\odot$)	$M_{\rm tot}$ (10^{14} M$_\odot$)	$f_{\rm gas}$
A520	$166.5 \pm^{6.0}_{7.2}$	$3.16 \pm^{0.22}_{0.25}$	$2.82 \pm^{0.31}_{0.35}$	$0.112 \pm^{0.006}_{0.005}$	$367.1 \pm^{9.3}_{9.2}$	$10.71 \pm^{0.30}_{0.29}$	$6.04 \pm^{0.47}_{0.44}$	$0.177 \pm^{0.009}_{0.009}$
Hot Slice	$168.1 \pm^{12.3}_{13.1}$	$3.18 \pm^{0.44}_{0.44}$	$2.90 \pm^{0.68}_{0.63}$	$0.109 \pm^{0.011}_{0.009}$	$375.5 \pm^{16.4}_{15.3}$	$11.60 \pm^{0.59}_{0.57}$	$6.47 \pm^{0.88}_{0.76}$	$0.179 \pm^{0.015}_{0.015}$
Cool Slice	$165.0 \pm^{8.7}_{10.9}$	$2.76 \pm^{0.29}_{0.34}$	$2.74 \pm^{0.46}_{0.51}$	$0.101 \pm^{0.008}_{0.006}$	$338.5 \pm^{14.5}_{14.9}$	$9.58 \pm^{0.56}_{0.58}$	$4.74 \pm^{0.63}_{0.60}$	$0.202 \pm^{0.016}_{0.014}$

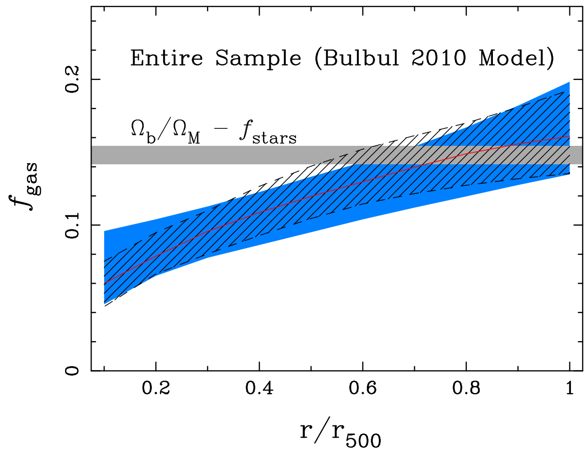

Figure 9. Average gas mass fraction profile for the Bulbul et al. (2010) model for all the clusters in the sample with $f_{\rm gas}(r_{500}) = 0.161 \pm 0.029$. The red line is the median and the hatched region is the 68.3% confidence interval. The blue envelope is the sample average $f_{\rm gas}$ using the Vikhlinin et al. (2006) model. The grey envelope is the difference of the cosmic baryon fraction and the fraction of baryons in stars and galaxies, $\Omega_{\rm b}/\Omega_{\rm M} - f_{\rm stars} = 0.148 \pm 0.006$ (Giodini et al. 2009; Komatsu et al. 2011).

Table 5. Systematic Uncertainties and Effects on $f_{\rm gas}$

Source	Effect on $f_{\rm gas}$	
	$f_{\rm gas}(r_{2500})$	$f_{\rm gas}(r_{500})$
Chandra Instrument Calibration		
–Surface Brightness	±1%	
–Temperature	±10%	
Hydrostatic Equilibrium	−8%	−10%
Spherical Symmetry Assumption	±6%	±8%
Modelling of X-ray Data	±6%	±1%
Clumping of Gas	···	−10%

mological value of $\Omega_{\rm b}/\Omega_{\rm M}$ even after accounting for a 10% reduction due to possible clumping of the gas.

7 COMPARISON WITH PREVIOUS STUDIES

7.1 Average gas mass fractions from Vikhlinin et al. 2006 and Arnaud et al. 2007

In this section we compare our result to previous studies of $f_{\rm gas}$ using hydrostatic mass estimates. We used the results from the samples of relaxed clusters by Vikhlinin et al. (2006, hereafter V06) and Arnaud et al. (2007, hereafter A07), and compare those results with our 13 relaxed clusters. V06 measured $f_{\rm gas}$ out to r_{500} for 10 relaxed clusters observed with *Chandra* spanning a redshift range $z = 0.02 - 0.23$, with a weighted average for these 10 clusters of

$$f_{\rm gas,\,V06} = 0.105 \pm 0.002.$$

The A07 sample consists of 10 relaxed clusters with $z \leqslant 0.15$ observed by *XMM-Newton*, with a weighted average for the 10 clusters of

$$f_{\rm gas,\,A07} = 0.106 \pm 0.004.$$

The sample used in this work are the most luminous clusters from the BCS and eBCS in the redshift range $0.15 \leqslant z \leqslant 0.30$ (Dahle 2006), with a weighted average for the 13 relaxed clusters of

$$f_{\rm gas,\,relaxed} = 0.150 \pm 0.004.$$

Notice that the value reported in Table 2 ($f_{\rm gas,\,relaxed} = 0.155 \pm 0.026$) is the value of the gas mass fraction for the average cluster profile, i.e., obtained from the combination of all Markov chains. In this section we use the weighted average of the 13 measurements for the relaxed clusters, since this number can be compared directly with the averages obtained from the data published in the V06 and A07 papers.

As an initial comparison, we checked for clusters used in our sample that were also analysed by V06 and A07. Clusters that overlap with our sample were *Abell 2390* (analysed in V06) and *Abell 2204* (analysed in A07). A07 found $f_{\rm gas}(r_{500}) = 0.126 \pm 0.013$ for *Abell 2204*, and we measure a value of 0.163 ± 0.010. Our temperature profiles do not agree, and comparison between the A07 result shown in Pointecouteau et al. (2005) and our Figure 4 indicate that our temperature profile has lower values at large radii. Since the temperature of the cluster is the dominant factor in calculating hydrostatic masses, the discrepancy in temperature profiles can be responsible for the different gas mass fractions. For *Abell 2390*, V06 calculates $f_{\rm gas}(r_{500}) = 0.141 \pm 0.009$. Our temperature profile agrees well with that of V06, and our measurement $f_{\rm gas}(r_{500}) = 0.131 \pm 0.024$ is also in very good agreement with V06.

7.2 Comparison with the Vikhlinin et al. 2006 results in a matching mass range

We also compared the masses of our cluster sample with those in the V06 and A07 samples. As seen in Figure 11, our clusters are generally more massive than those in the V06 or A07 samples, yet there is an overlap in the range of masses for all three samples. To compare clusters in a similar mass range, we grouped clusters in two bins: bin 1 includes clusters in the mass range $2 < M_{\rm tot} < 5 \times 10^{14}M_\odot$, and bin 2 with $M_{\rm tot} > 5 \times 10^{14}M_\odot$. The weighted average of $f_{\rm gas}$

Table 4. Vikhlinin et al. (2006) and Bulbul et al. (2010) Model Comparison of Sample Average Cluster Properties

Model	r_{2500} (arcsec)	$M_{\rm gas}$ (10^{13} M$_\odot$)	$M_{\rm tot}$ (10^{14} M$_\odot$)	$f_{\rm gas}$
Vikhlinin et al. (2006)	137.4 ± 34.7	2.80 ± 1.50	2.53 ± 1.38	0.110 ± 0.017
Bulbul et al. (2010)	132.4 ± 27.7	2.73 ± 1.05	2.36 ± 0.96	0.115 ± 0.016
Model	**r_{500} (arcsec)**	**$M_{\rm gas}$ (10^{13} M$_\odot$)**	**$M_{\rm tot}$ (10^{14} M$_\odot$)**	**$f_{\rm gas}$**
Vikhlinin et al. (2006)	292.2 ± 71.1	8.07 ± 3.28	5.05 ± 2.43	0.163 ± 0.032
Bulbul et al. (2010)	301.2 ± 59.4	8.57 ± 2.78	5.58 ± 2.26	0.161 ± 0.029

for these bins are reported in Table 6, showing that there is a significant difference between our $f_{\rm gas}$ measurements and those of V06 and A07, especially for bin 1. Also, contrary to V06 and A07, our results do not show an increase in $f_{\rm gas}$ with mass between the two mass bins.

To further investigate this disagreement, we decided to analyse all of the V06 clusters that did not require *ROSAT* data for the measurement of the background, namely A133, A1413, A383, and A907 (Vikhlinin et al. 2006). We extracted temperature profiles and obtained surface brightness profiles for these four clusters, and then measured masses, using the same reduction and analysis procedure as for all other clusters in this work. Our weighted average for the four clusters is 0.114 ± 0.006 (see Table 7). This is in agreement with the results from V06, who measure a value of 0.109 ± 0.003 for these clusters. We therefore conclude that, on average, our method of analysis yields statistically consistent results to those of V06.

Of the four clusters in this comparison sample, three are in agreement at the 1σ level. The only cluster we do not find statistical agreement with is A1413: we measure $f_{\rm gas}(r_{500}) = 0.161 \pm 0.011$, whereas V06 reports 0.107 ± 0.007. Since the temperature we obtain for A1413 at large radii is lower than that of V06, we conclude that this is likely the reason for the disagreement, since a lower temperature would result in a lower total mass and thus a higher gas mass fraction. Differences in the *Chandra* calibration or other aspects of the data analysis are likely responsible for the disagreement between our results and those of V06 for A1413. We also note that A07 also analysed A1413 and measured $f_{\rm gas}(r_{500}) = 0.157 \pm 0.015$, which is in very good agreement with our value.

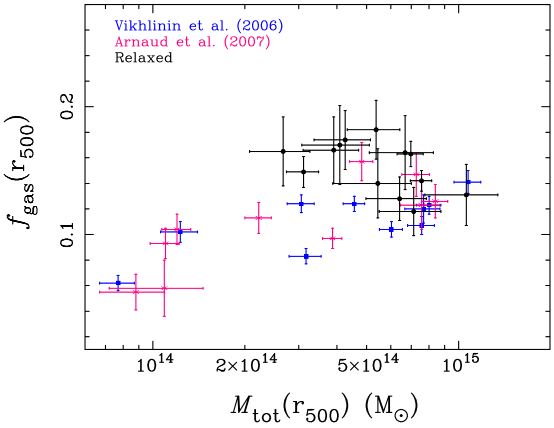

Figure 11. $f_{\rm gas} - M$ plot for Vikhlinin et al. (2006), Arnaud et al. (2007), and the relaxed clusters from this work. The mass ranges show overlap between the samples.

7.3 A possible luminosity–selection bias for the gas mass fraction

The sample of 35 clusters used in this work was selected as the most X-ray luminous in the $0.15 - 0.30$ redshift range. We calculated the X-ray luminosity in the $0.6 - 9.0$ keV band using spectra within the $(0.15 - 1)\,r_{500}$ region (Giles et al. 2012). We compare the $L_{\rm X}$ for the five relaxed clusters in bin 1 of our sample, and the three clusters (A133, A383, and A907) from the V06 sample in the same mass range. A133, A383, and A907 were found to have luminosity of respectively 5.5×10^{43}, 2.8×10^{44}, and 3.8×10^{44} erg s^{-1}, for an average of 2.4×10^{44} erg s^{-1}, a factor of approximately *three times lower* than the values for the five clusters in the same mass range present in our sample (Table 6). This analysis of clusters in the same mass range indicates that the selection of clusters based on X-ray luminosity – as in the case of our sample – may result in the preferential selection of the high-$f_{\rm gas}$ tail of the cluster $f_{\rm gas}$ distribution for a given mass. This is not surprising, since both $f_{\rm gas}$ and $L_{\rm X}$ depend on the gas mass content of the cluster. This conclusion is also supported by the scaling relations measured by Giles et al. (2012), in which we use the same sample of high-$L_{\rm X}$ clusters to find that there is an offset with respect to earlier studies that can be explained by a higher gas mass for a fixed total mass.

8 DISCUSSION AND CONCLUSIONS

In this paper we studied the gas mass fraction for the 35 most luminous clusters in the BCS/eBCS at redshift $z = 0.15 - 0.30$ (Dahle 2006). In accord with earlier studies, we find that the gas mass fraction increases with radius, and thus the value of $f_{\rm gas}$ depends on the radius used.

Low gas mass fractions (e.g., $f_{\rm gas} \leqslant 0.1$) have been observed in groups of galaxies (Sun et al. 2009), likely because the gas is not fully bound to the group due to the shallow gravitational potential. Recent studies report that the cluster baryon fraction falls short of the cosmic baryon fraction at r_{500} even in more massive clusters (e.g., Vikhlinin et al. 2006; Arnaud et al. 2007; Ettori et al. 2009; Rasheed et al. 2010). In our sample of the most X-ray luminous clusters at redshift $z = 0.15 - 0.30$, we find a significantly higher average

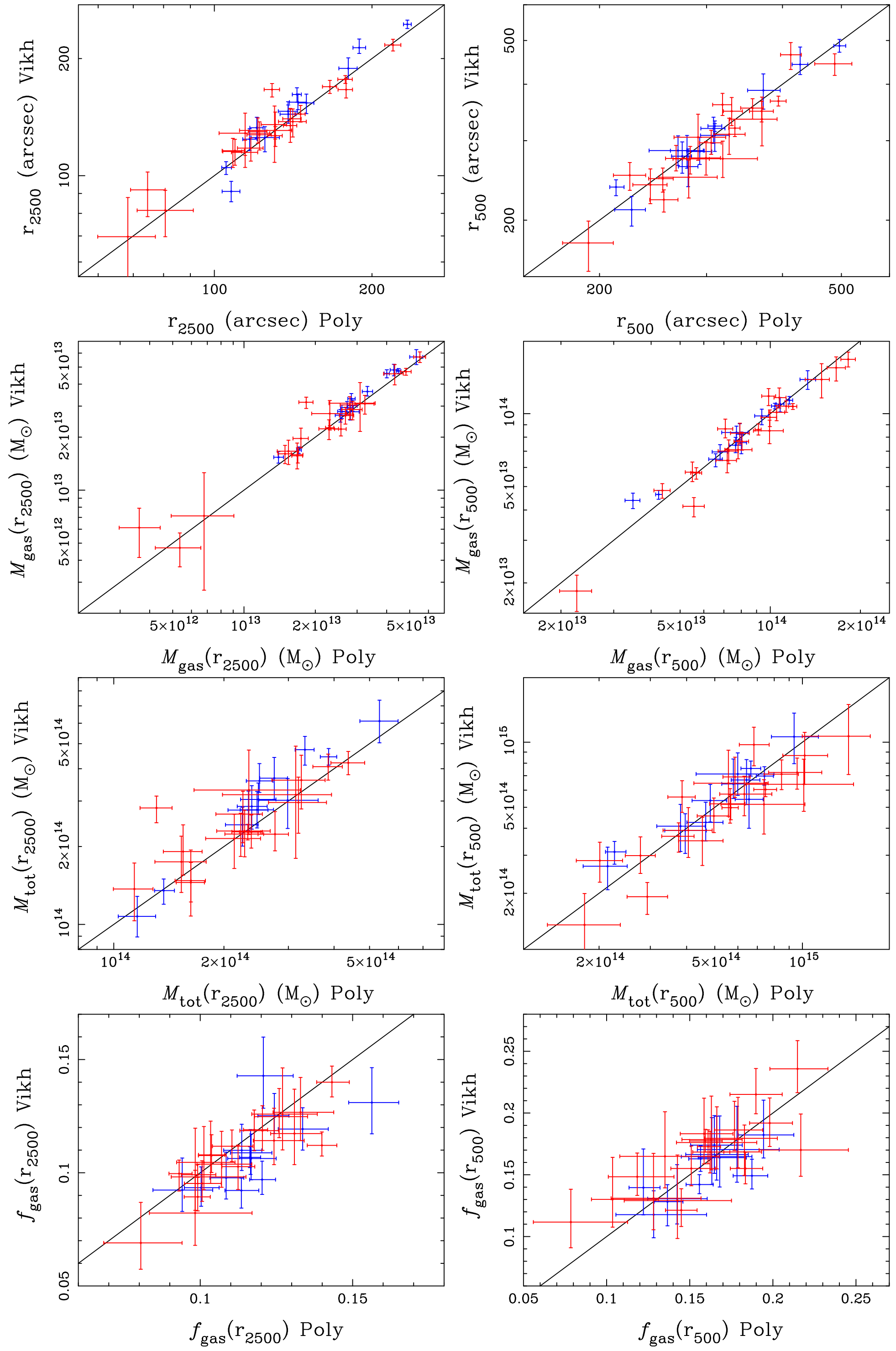

Figure 10. Comparison between measurements using the Vikhlinin et al. (2006) (Vikh) and Bulbul et al. (2010) (Poly) models. The black line is $y = x$, unrelaxed clusters are shown in red, and the blue data points correspond to relaxed clusters.

value of the gas mass fraction at r_{500}, $f_{\rm gas} = 0.163 \pm 0.032$. To find the total baryon fraction we used the stellar fraction from Giodini et al. (2009) and Gonzalez et al. (2007). Comparing the total baryon fraction with the cosmic baryon fraction ($\Omega_{\rm b}/\Omega_{\rm M} = 0.167 \pm 0.006$) we find that the two measurements agree at the 1σ level, i.e., the gas mass fraction at r_{500} is in fact consistent with the cosmological value of $\Omega_{\rm b}/\Omega_{\rm M}$, and there are no *missing baryons* within r_{500} in the most luminous and massive clusters. A recent study by Miller et al. (2012) also find a gas mass fraction in agreement with the cosmic baryon fraction using data from *Chandra*, *XMM-Newton*, and *Suzaku*.

One question that remains open is: what happens to $f_{\rm gas}$ beyond r_{500}? As seen in Figure 5, the gas mass fraction

Table 6. Cluster Properties for Mass Bin 1 ($2 < M_{\rm tot} < 5 \times 10^{14}$ M$_\odot$) and Mass Bin 2 ($M_{\rm tot} > 5 \times 10^{14}$ M$_\odot$)

Sample	$f_{\rm gas}(r_{500})$		Number of Clusters		$L_{\rm X}$
	Bin 1	Bin 2	Bin 1	Bin 2	Bin 1 (10^{44} erg s^{-1})
Vikhlinin et al. (2006)	0.109 ± 0.004	0.116 ± 0.003	3	5	2.4
Arnaud et al. (2007)	0.111 ± 0.006	0.131 ± 0.009	3	3	···
Relaxed Clusters	0.158 ± 0.009	0.147 ± 0.005	5	8	7.1

Table 7. Comparison of Clusters with Vikhlinin et al. (2006)

Cluster	r_{500} (kpc)	$M_{\rm tot}(r_{2500})$ (10^{14} M$_\odot$)	$f_{\rm gas}(r_{2500})$	$M_{\rm tot}(r_{500})$ (10^{14} M$_\odot$)	$f_{\rm gas}(r_{500})$	Weighted Avg. $f_{\rm gas}(r_{500})$
			Vikhlinin et al. (2006)			
A133	1007 ± 41	1.13 ± 0.07	0.067 ± 0.002	3.17 ± 0.38	0.083 ± 0.006	0.109 ± 0.003
A1413	1299 ± 43	3.01 ± 0.18	0.094 ± 0.003	7.57 ± 0.76	0.107 ± 0.007	
A383	944 ± 32	1.64 ± 0.14	0.092 ± 0.005	3.06 ± 0.31	0.124 ± 0.007	
A907	1096 ± 30	2.21 ± 0.14	0.091 ± 0.003	4.56 ± 0.37	0.124 ± 0.006	
			Landry et al. (2012)			
A133	1027 ± 48	1.11 ± 0.07	0.066 ± 0.002	3.26 ± 0.46	0.080 ± 0.008	0.114 ± 0.006
A1413	1160 ± 40	3.55 ± 0.45	0.097 ± 0.007	5.06 ± 0.52	0.161 ± 0.011	
A383	886 ± 98	1.40 ± 0.46	0.120 ± 0.022	2.36 ± 0.79	0.169 ± 0.045	
A907	1142 ± 53	2.19 ± 0.12	0.104 ± 0.003	4.91 ± 0.67	0.132 ± 0.013	

increases with radius. A naive extrapolation beyond r_{500} will give an even higher value for the gas mass fraction. The total baryon fraction in this case will be greater than the cosmological value, $\Omega_{\rm b}/\Omega_{\rm M}$. High values of the gas mass fractions towards the virial radius have been reported in recent studies based on *Suzaku* data (e.g., Simionescu et al. 2011). However, there are two important reasons why simple extrapolations to large radii of the measured radial trend of $f_{\rm gas}(r)$ may not be valid. First, the gas beyond r_{500} is not likely to be in hydrostatic equilibrium. Non-thermal pressure support will become more significant at radii $> r_{500}$ and will impact the measurement of the total mass (Nagai et al. 2007; Lau et al. 2009). An increase of non-thermal pressure support would cause an underestimate of total mass, and thus an overestimate of $f_{\rm gas}$. Therefore, the true gas mass fraction would be lower than our measured value in the presence of non-thermal pressure. The second reason is that clumping of the gas may also become more important at large radii. Observations and simulations show that the gas clumping factor increases beyond r_{500} and will considerably bias X-ray mass measurements (Nagai & Lau 2011; Simionescu et al. 2011; Eckert et al. 2012). As a result of clumping, the true gas mass fraction at large radii would be lower than the value measured assuming a smooth distribution of the gas.

We also consider the effect that our sample selection criteria could have on the measurement of $f_{\rm gas}$. The sample presented in this paper comprises clusters selected because of their high X-ray flux and luminosity, i.e., our sample preferentially selects clusters with a high $L_{\rm X}$ for a given mass. Since $L_{\rm X}$ depends on the gas mass, a luminosity-selected sample may have a larger fraction of clusters with high $f_{\rm gas}$ than samples selected with other criteria. The extent of any such bias would depend on the correlation between the scatter in $f_{\rm gas}$ and $L_{\rm X}$ at fixed mass, and the magnitude of the intrinsic scatter in $f_{\rm gas}$. Full account of this effect requires modelling of the selection function and population scatter of the sample, which is presented in Giles et al. (2012). For the current study, we estimate the intrinsic scatter of $f_{\rm gas}$ in our sample as $11\% \pm 4\%$. This may be underestimated if clusters from the low $f_{\rm gas}$ tail of the distribution are excluded by the luminosity selection of the sample. If this bias exists, then it could pose problems for using the gas mass fraction for cosmology. In fact, clusters used for cosmological applications are generally selected on the basis of their high luminosity, allowing their study at high redshift. Such clusters would be biased towards high $f_{\rm gas}$, potentially distorting the cosmological constraints derived from the $f_{\rm gas}(z)$ tests. The implication is that complete (or at least statistically representative) samples should be used for the $f_{\rm gas}(z)$ tests, so that the selection bias can be corrected. While these samples would necessarily contain morphologically disturbed clusters, our results show that $f_{\rm gas}$ measurements are not significantly affected by cluster morphology, at least out to r_{500}; Giles et al. (2012) also find an agreement between scaling relations for relaxed and unrelaxed hydrostatic masses. This suggests that complete samples of clusters could be used for $f_{\rm gas}(z)$ tests. A complementary approach would be to study the baryon fraction of clusters selected independently of the ICM (e.g., red sequence or weak lensing selected clusters). This would give a measurement of the range of baryon fractions that is free from selection biases associated with their X-ray emission.

We conclude that the large value of $f_{\rm gas}$ at r_{500} measured for this sample is representative of the high-$f_{\rm gas}$ tail of the cluster population, and that the most massive and X-ray luminous clusters in this redshift range have the cosmological ratio of baryons to dark matter even at r_{500}.

Table 8. Vikhlinin et al. (2006) Model Density Parameters

Cluster	$n_{\rm e0}$ (10^{-2} cm^{-3})	$r_{\rm c}$ (arcsec)	β	$r_{\rm s}$ (arcsec)	ε	$n_{\rm e02}$	γ	α
A115	$5.86 \pm^{0.72}_{0.77}$	$4.89 \pm^{0.72}_{0.60}$	$0.42 \pm^{0.01}_{0.01}$	$751.40 \pm^{305.30}_{242.50}$	$2.01 \pm^{1.15}_{1.14}$	0.0	3.0	0.0
A1423	$2.58 \pm^{0.19}_{0.17}$	$9.85 \pm^{0.82}_{0.83}$	$0.44 \pm^{0.01}_{0.01}$	$280.80 \pm^{110.30}_{110.90}$	$0.90 \pm^{0.63}_{0.40}$	0.0	3.0	0.0
A1576	$1.16 \pm^{0.14}_{0.12}$	$23.33 \pm^{3.21}_{3.13}$	$0.53 \pm^{0.02}_{0.02}$	100.0	0.0	0.0	3.0	0.0
A1682	$0.64 \pm^{0.10}_{0.07}$	$20.19 \pm^{6.17}_{6.06}$	$0.33 \pm^{0.04}_{0.05}$	$190.80 \pm^{47.41}_{55.52}$	$2.33 \pm^{0.67}_{0.54}$	0.0	3.0	0.0
A1758	$0.37 \pm^{0.01}_{0.01}$	$81.45 \pm^{2.14}_{2.14}$	0.7	100.0	0.0	0.0	3.0	0.0
A1763	$0.81 \pm^{0.03}_{0.03}$	$35.77 \pm^{2.74}_{2.63}$	$0.48 \pm^{0.02}_{0.02}$	$425.10 \pm^{78.03}_{49.17}$	3.0	0.0	3.0	0.0
A1835	$9.84 \pm^{0.17}_{0.17}$	$6.69 \pm^{0.14}_{0.13}$	$0.50 \pm^{0.00}_{0.00}$	$123.10 \pm^{8.79}_{7.47}$	$1.18 \pm^{0.07}_{0.07}$	0.0	3.0	0.0
A1914	$1.47 \pm^{0.05}_{0.05}$	$54.80 \pm^{2.55}_{2.43}$	$0.73 \pm^{0.02}_{0.02}$	500.0	0.0	0.0	3.0	0.0
A2111	$0.60 \pm^{0.02}_{0.02}$	$42.10 \pm^{2.31}_{2.43}$	$0.54 \pm^{0.01}_{0.02}$	10.0	0.0	0.0	3.0	0.0
A2204	$30.10 \pm^{1.54}_{1.73}$	$3.71 \pm^{0.19}_{0.16}$	$0.46 \pm^{0.00}_{0.00}$	$133.00 \pm^{9.62}_{8.80}$	$1.12 \pm^{0.06}_{0.06}$	0.0	3.0	0.0
A2219	$0.90 \pm^{0.04}_{0.04}$	$59.85 \pm^{3.51}_{3.53}$	$0.63 \pm^{0.02}_{0.02}$	500.0	0.0	0.0	3.0	0.0
A2261	$3.10 \pm^{0.15}_{0.17}$	$13.44 \pm^{2.53}_{1.43}$	$0.44 \pm^{0.06}_{0.04}$	$70.00 \pm^{44.92}_{14.46}$	$0.98 \pm^{0.15}_{0.17}$	0.0	3.0	0.0
A2390	$7.64 \pm^{1.45}_{1.06}$	$3.86 \pm^{0.77}_{0.81}$	$0.36 \pm^{0.01}_{0.01}$	$145.10 \pm^{13.73}_{12.32}$	$2.67 \pm^{0.27}_{0.23}$	0.0	3.0	0.0
A2552	$1.74 \pm^{0.20}_{0.19}$	$9.42 \pm^{3.38}_{2.53}$	$0.29 \pm^{0.06}_{0.05}$	$51.24 \pm^{9.26}_{8.05}$	$1.57 \pm^{0.26}_{0.37}$	0.0	3.0	0.0
A2631	$0.57 \pm^{0.02}_{0.02}$	$51.52 \pm^{8.06}_{6.09}$	$0.55 \pm^{0.09}_{0.07}$	$178.90 \pm^{77.79}_{40.74}$	2.0	0.0	3.0	0.0
A267	$0.93 \pm^{0.05}_{0.05}$	$35.98 \pm^{2.70}_{2.61}$	$0.64 \pm^{0.02}_{0.03}$	100.0	0.0	0.0	3.0	0.0
A520	$0.37 \pm^{0.01}_{0.01}$	$127.30 \pm^{7.30}_{6.53}$	$0.85 \pm^{0.04}_{0.04}$	900.0	0.0	0.0	3.0	0.0
A586	$1.63 \pm^{0.04}_{0.04}$	$31.30 \pm^{0.96}_{0.98}$	$0.61 \pm^{0.01}_{0.01}$	10.0	0.0	0.0	3.0	0.0
A611	$2.14 \pm^{0.11}_{0.10}$	$16.59 \pm^{1.16}_{1.10}$	$0.56 \pm^{0.02}_{0.02}$	$426.30 \pm^{134.30}_{107.50}$	5.0	0.0	3.0	0.0
A665	$1.00 \pm^{0.05}_{0.05}$	$23.04 \pm^{1.63}_{1.52}$	$0.41 \pm^{0.01}_{0.01}$	$472.20 \pm^{23.93}_{22.77}$	5.0	0.0	3.0	0.0
A68	$0.82 \pm^{0.13}_{0.08}$	$43.14 \pm^{9.30}_{15.41}$	$0.62 \pm^{0.10}_{0.19}$	$233.40 \pm^{110.30}_{104.50}$	$2.98 \pm^{1.58}_{1.76}$	0.0	3.0	0.0
A697	$0.90 \pm^{0.07}_{0.07}$	$43.42 \pm^{6.02}_{6.59}$	$0.58 \pm^{0.04}_{0.07}$	$279.30 \pm^{159.40}_{162.50}$	$1.04 \pm^{0.83}_{0.72}$	0.0	3.0	0.0
A773	$0.87 \pm^{0.02}_{0.02}$	$45.61 \pm^{1.23}_{1.21}$	$0.62 \pm^{0.01}_{0.01}$	100.0	0.0	0.0	3.0	0.0
A781	$0.27 \pm^{0.02}_{0.02}$	$111.40 \pm^{4.74}_{4.52}$	0.9	500.0	0.0	0.0	3.0	0.0
A963	$2.57 \pm^{0.14}_{0.14}$	$12.66 \pm^{1.17}_{1.09}$	$0.43 \pm^{0.01}_{0.01}$	$176.10 \pm^{18.50}_{20.74}$	$3.05 \pm^{0.33}_{0.43}$	0.0	3.0	0.0
MS 1455.0+2232	$7.30 \pm^{0.37}_{0.34}$	$11.47 \pm^{0.68}_{0.71}$	$0.45 \pm^{0.00}_{0.00}$	$4.96 \pm^{0.85}_{0.62}$	1.0	0.0	3.0	0.0
RX J0437.1+0043	$4.07 \pm^{0.37}_{0.29}$	$6.48 \pm^{0.91}_{0.93}$	$0.38 \pm^{0.03}_{0.03}$	$48.88 \pm^{9.53}_{7.39}$	$1.35 \pm^{0.16}_{0.15}$	0.0	3.0	0.0
RX J0439.0+0715	$3.06 \pm^{0.73}_{0.64}$	$8.69 \pm^{4.49}_{2.90}$	$0.38 \pm^{0.06}_{0.06}$	$108.40 \pm^{47.30}_{31.81}$	$2.29 \pm^{0.51}_{0.41}$	0.0	3.0	0.0
RX J1720.1+2638	$7.37 \pm^{0.26}_{0.22}$	$9.38 \pm^{0.54}_{0.50}$	$0.48 \pm^{0.01}_{0.01}$	$97.82 \pm^{19.53}_{13.87}$	$0.92 \pm^{0.07}_{0.07}$	0.0	3.0	0.0
RX J2129.6+0005	$6.43 \pm^{0.43}_{0.38}$	$6.72 \pm^{0.67}_{0.62}$	$0.44 \pm^{0.02}_{0.02}$	$76.71 \pm^{21.93}_{15.13}$	$1.12 \pm^{0.15}_{0.12}$	0.0	3.0	0.0
Z2089	$11.21 \pm^{1.92}_{1.55}$	$5.46 \pm^{1.17}_{1.18}$	$0.54 \pm^{0.03}_{0.05}$	$99.43 \pm^{182.70}_{51.51}$	1.0	0.0	3.0	0.0
Z3146	$10.49 \pm^{0.33}_{0.34}$	$6.89 \pm^{0.27}_{0.27}$	$0.50 \pm^{0.01}_{0.01}$	$96.05 \pm^{10.79}_{9.96}$	$1.56 \pm^{0.18}_{0.17}$	0.0	3.0	0.0
Z5247	$0.19 \pm^{0.01}_{0.01}$	$84.60 \pm^{6.46}_{5.82}$	0.5	100.0	0.0	0.0	3.0	0.0
Z5768	$0.63 \pm^{0.15}_{0.14}$	$15.49 \pm^{5.89}_{3.74}$	$0.45 \pm^{0.05}_{0.04}$	100.0	0.0	0.0	3.0	0.0
Z7215	$0.62 \pm^{0.07}_{0.06}$	$51.41 \pm^{9.43}_{7.84}$	$0.76 \pm^{0.09}_{0.07}$	500.0	0.0	0.0	3.0	0.0

Table 9. Vikhlinin et al. (2006) Model Temperature Parameters

Cluster	T_0 (keV)	$T_{\rm min}$ (keV)	$r_{\rm cool}$ (arcsec)	$a_{\rm cool}$	$r_{\rm t}$ (arcsec)	a	b	c	$\chi^2_{\rm tot}$(d.o.f.)
A115	$21.94 \pm^{7.07}_{5.74}$	$2.08 \pm^{0.36}_{0.39}$	$222.50 \pm^{71.81}_{78.68}$	1.0	$307.60 \pm^{82.31}_{72.12}$	0.0	2.0	2.0	92.50 (128)
A1423	$7.47 \pm^{1.69}_{1.26}$	$4.98 \pm^{1.03}_{1.06}$	50.0	2.0	$183.80 \pm^{97.22}_{66.96}$	0.0	2.0	1.0	56.65 (113)
A1576	$9.20 \pm^{2.48}_{1.69}$	9.20	50.0	1.0	$411.50 \pm^{373.90}_{260.90}$	0.0	1.0	1.0	16.80 (74)
A1682	$8.91 \pm^{2.55}_{1.73}$	2.0	$16.43 \pm^{8.94}_{8.94}$	2.0	$121.70 \pm^{71.64}_{40.70}$	0.0	2.0	1.0	52.65 (89)
A1758	$10.40 \pm^{2.47}_{2.34}$	10.40	10.0	0.0	100.0	0.0	1.0	0.0	104.51 (59)
A1763	$8.97 \pm^{1.03}_{1.03}$	8.97	50.0	1.0	1200.0	0.0	1.0	1.0	97.75 (126)
A1835	$21.98 \pm^{9.31}_{5.26}$	3.0	$51.01 \pm^{23.25}_{13.88}$	1.0	$307.10 \pm^{256.50}_{80.36}$	0.0	$1.14 \pm^{0.52}_{0.34}$	2.0	196.64 (83)
A1914	$11.38 \pm^{1.91}_{1.27}$	11.38	50.0	1.0	$487.00 \pm^{350.70}_{227.60}$	0.0	1.0	1.0	66.00 (109)
A2111	$8.43 \pm^{1.86}_{1.40}$	6.0	50.0	1.0	$469.30 \pm^{306.20}_{184.80}$	0.0	2.0	2.0	43.95 (93)
A2204	$9.94 \pm^{0.59}_{0.49}$	$0.09 \pm^{0.10}_{0.06}$	$7.78 \pm^{0.69}_{0.62}$	2.0	$636.70 \pm^{329.60}_{187.00}$	0.0	$1.94 \pm^{0.57}_{0.48}$	2.0	153.68 (136)
A2219	$14.16 \pm^{2.41}_{1.87}$	14.16	50.0	1.0	$305.60 \pm^{230.50}_{120.80}$	0.0	1.0	1.0	21.66 (104)
A2261	$11.66 \pm^{1.72}_{1.39}$	4.0	30.0	0.5	$299.80 \pm^{117.60}_{80.10}$	0.0	2.0	2.0	73.71 (105)
A2390	$30.11 \pm^{4.55}_{4.27}$	0.0	60.0	$0.61 \pm^{0.12}_{0.13}$	1000.0	0.0	1.0	$4.00 \pm^{1.59}_{1.30}$	87.44 (152)
A2552	$8.77 \pm^{1.17}_{1.23}$	8.77	10.0	0.0	300.0	0.0	2.0	2.0	61.66 (74)
A2631	$9.36 \pm^{1.97}_{1.43}$	9.36	10.0	0.0	$316.80 \pm^{239.40}_{149.70}$	0.0	1.0	1.0	29.95 (74)
A267	$5.08 \pm^{0.91}_{0.86}$	5.08	10.0	0.0	$385.30 \pm^{385.50}_{143.80}$	0.0	2.0	2.0	122.55 (152)
A520	$8.76 \pm^{0.55}_{0.58}$	8.76	3.0	1.0	$346.50 \pm^{45.52}_{37.64}$	0.0	2.0	2.0	43.71 (128)
A586	$8.83 \pm^{0.76}_{0.74}$	5.0	60.0	0.2	$330.30 \pm^{88.25}_{64.65}$	0.0	2.0	2.0	49.60 (103)
A611	$9.86 \pm^{1.33}_{1.57}$	5.0	20.0	1.0	300.0	0.0	2.0	2.0	26.61 (47)
A665	$11.71 \pm^{2.86}_{2.02}$	$6.41 \pm^{1.17}_{1.27}$	100.0	1.0	$510.40 \pm^{206.40}_{155.30}$	0.0	2.0	2.0	180.08 (179)
A68	$10.08 \pm^{3.95}_{2.06}$	10.08	50.0	1.0	$269.60 \pm^{450.00}_{161.60}$	0.0	1.0	1.0	23.82 (78)
A697	$13.87 \pm^{3.86}_{2.52}$	6.0	$38.38 \pm^{29.42}_{22.40}$	2.0	$407.10 \pm^{334.20}_{208.70}$	0.0	1.0	1.0	29.05 (117)
A773	$7.73 \pm^{0.81}_{0.66}$	7.73	10.0	0.0	1000.0	0.0	1.0	1.0	127.68 (94)
A781	$6.53 \pm^{1.13}_{1.12}$	6.53	50.0	0.0	1000.0	0.0	1.0	1.0	34.04 (75)
A963	$10.65 \pm^{2.04}_{1.35}$	3.0	20.0	1.0	$98.05 \pm^{26.23}_{30.87}$	0.0	2.0	1.0	76.59 (77)
MS 1455.0+2232	$4.91 \pm^{0.38}_{0.42}$	$3.87 \pm^{0.66}_{0.63}$	20.0	2.0	2000.0	0.0	2.0	2.0	150.82 (102)
RX J0437.1+0043	$10.38 \pm^{2.08}_{1.63}$	$3.28 \pm^{1.13}_{1.38}$	30.0	1.0	$278.90 \pm^{197.90}_{102.60}$	0.0	2.0	2.0	49.92 (57)
RX J0439.0+0715	$11.54 \pm^{2.15}_{1.77}$	3.0	50.0	1.0	$190.50 \pm^{54.50}_{50.20}$	0.0	2.0	2.0	14.34 (90)
RX J1720.1+2638	$13.94 \pm^{2.77}_{2.14}$	$4.37 \pm^{0.41}_{0.44}$	$73.39 \pm^{13.89}_{12.59}$	2.0	$363.80 \pm^{237.70}_{145.00}$	0.0	1.0	1.0	163.51 (101)
RX J2129.6+0005	$9.43 \pm^{2.19}_{1.43}$	$4.19 \pm^{0.71}_{0.82}$	$32.80 \pm^{17.64}_{14.19}$	2.0	$141.70 \pm^{70.04}_{41.80}$	0.0	2.0	1.0	44.31 (74)
Z2089	$4.86 \pm^{0.98}_{0.85}$	3.5	50.0	$0.70 \pm^{0.63}_{0.49}$	$942.70 \pm^{698.10}_{688.10}$	0.0	2.0	2.0	6.93 (43)
Z3146	$10.39 \pm^{4.10}_{1.85}$	2.0	$18.84 \pm^{20.45}_{8.12}$	1.0	$265.40 \pm^{165.40}_{92.45}$	0.0	2.0	2.0	98.22 (90)
Z5247	$7.15 \pm^{2.41}_{1.57}$	7.15	50.0	0.0	$241.50 \pm^{328.00}_{129.00}$	0.0	1.0	1.0	43.82 (82)
Z5768	$4.55 \pm^{1.10}_{1.17}$	4.55	50.0	0.0	500.0	0.0	1.0	1.0	29.35 (59)
Z7215	$8.68 \pm^{2.12}_{1.73}$	2.0	$17.11 \pm^{12.23}_{10.23}$	2.0	300.0	0.0	2.0	2.0	18.15 (59)

Table 10. Bulbul et al. (2010) Model Parameters

Cluster	$n_{\rm e0}$ (10^{-2} cm^{-3})	$r_{\rm s}$ (arcsec)	n	$\beta + 1$	T_0 (keV)	$r_{\rm cool}$ (arcsec)	ξ	$a_{\rm cool}$	$\chi^2_{\rm tot}$(d.o.f.)
A115	$0.80 \pm^{0.16}_{0.12}$	$22.54 \pm^{7.27}_{5.20}$	$6.72 \pm^{2.33}_{1.71}$	$2.27 \pm^{0.12}_{0.08}$	$10.62 \pm^{1.00}_{0.98}$	$29.82 \pm^{2.63}_{2.64}$	$0.16 \pm^{0.03}_{0.03}$	2.0	89.66 (130)
A1423	$0.60 \pm^{0.14}_{0.14}$	$42.07 \pm^{26.91}_{17.53}$	$2.08 \pm^{0.50}_{0.44}$	$3.28 \pm^{0.86}_{0.44}$	$18.50 \pm^{3.22}_{3.24}$	$42.83 \pm^{10.77}_{6.65}$	$0.17 \pm^{0.04}_{0.04}$	$1.39 \pm^{0.19}_{0.22}$	57.13 (113)
A1576	$1.81 \pm^{0.23}_{0.16}$	$20.77 \pm^{4.47}_{4.70}$	$4.91 \pm^{1.04}_{1.20}$	$2.53 \pm^{0.18}_{0.11}$	$11.95 \pm^{2.05}_{1.52}$	10.0	1.0	2.0	14.22 (74)
A1682	$0.41 \pm^{0.08}_{0.05}$	$272.60 \pm^{135.90}_{130.10}$	4.0	$3.95 \pm^{0.69}_{0.69}$	$9.39 \pm^{0.80}_{0.80}$	$33.84 \pm^{13.17}_{10.14}$	$0.56 \pm^{0.11}_{0.07}$	2.0	63.18 (92)
A1758	$0.51 \pm^{0.02}_{0.02}$	$347.10 \pm^{9.29}_{9.04}$	10.0	3.0	$11.66 \pm^{1.20}_{2.21}$	10.0	1.0	2.0	115.65 (59)
A1763	$1.17 \pm^{0.06}_{0.06}$	$41.05 \pm^{5.47}_{4.18}$	10.0	$2.27 \pm^{0.02}_{0.01}$	$9.66 \pm^{0.93}_{0.54}$	10.0	1.0	1.0	121.18 (127)
A1835	$4.52 \pm^{0.37}_{0.47}$	$14.63 \pm^{1.74}_{1.18}$	$8.99 \pm^{1.53}_{1.64}$	$2.29 \pm^{0.07}_{0.05}$	$11.91 \pm^{0.92}_{0.73}$	$16.11 \pm^{0.63}_{0.43}$	$0.44 \pm^{0.03}_{0.04}$	$3.58 \pm^{0.43}_{0.39}$	83.43 (84)
A1914	$2.27 \pm^{0.10}_{0.10}$	$77.65 \pm^{12.41}_{9.79}$	$7.96 \pm^{4.24}_{2.30}$	$2.56 \pm^{0.29}_{0.21}$	$12.08 \pm^{1.45}_{1.13}$	10.0	1.0	2.0	108.39 (109)
A2111	$0.90 \pm^{0.04}_{0.03}$	$42.98 \pm^{4.65}_{4.03}$	$34.45 \pm^{11.97}_{16.97}$	$2.08 \pm^{0.08}_{0.02}$	$7.24 \pm^{0.55}_{0.55}$	$2.18 \pm^{1.53}_{0.92}$	1.0	$6.04 \pm^{1.43}_{1.61}$	60.46 (91)
A2204	$4.15 \pm^{0.22}_{0.26}$	$22.56 \pm^{1.74}_{1.61}$	$6.60 \pm^{1.00}_{0.79}$	$2.39 \pm^{0.06}_{0.06}$	$15.07 \pm^{1.02}_{0.77}$	$19.83 \pm^{0.72}_{0.56}$	$0.17 \pm^{0.01}_{0.01}$	2.0	123.22 (139)
A2219	$1.38 \pm^{0.07}_{0.07}$	$82.36 \pm^{16.16}_{10.90}$	$4.93 \pm^{1.86}_{0.84}$	$2.81 \pm^{0.26}_{0.26}$	$14.79 \pm^{1.22}_{1.29}$	10.0	1.0	2.0	32.25 (104)
A2261	$2.84 \pm^{0.53}_{0.59}$	$18.29 \pm^{5.75}_{3.27}$	$5.19 \pm^{1.40}_{1.30}$	$2.48 \pm^{0.21}_{0.12}$	$13.53 \pm^{2.41}_{1.64}$	$53.57 \pm^{19.95}_{10.70}$	$0.68 \pm^{0.08}_{0.10}$	2.0	75.54 (105)
A2390	$1.09 \pm^{0.11}_{0.08}$	$155.40 \pm^{43.66}_{39.02}$	$3.60 \pm^{0.74}_{0.50}$	$3.95 \pm^{0.69}_{0.59}$	$19.47 \pm^{1.30}_{1.35}$	$21.91 \pm^{2.14}_{2.12}$	$0.19 \pm^{0.02}_{0.02}$	2.0	99.80 (153)
A2552	$2.24 \pm^{0.13}_{0.12}$	$17.51 \pm^{2.12}_{1.84}$	15.0	$2.16 \pm^{0.01}_{0.01}$	$9.17 \pm^{0.71}_{0.89}$	10.0	1.0	2.0	69.04 (76)
A2631	$0.76 \pm^{0.02}_{0.02}$	$404.00 \pm^{159.20}_{121.30}$	$4.56 \pm^{1.98}_{0.88}$	$5.39 \pm^{1.63}_{1.68}$	$9.82 \pm^{1.27}_{1.22}$	20.0	1.0	2.0	30.22 (75)
A267	$1.42 \pm^{0.09}_{0.08}$	$57.45 \pm^{14.89}_{12.49}$	$3.40 \pm^{1.12}_{0.64}$	$3.35 \pm^{0.55}_{0.46}$	$7.78 \pm^{1.01}_{1.10}$	20.0	1.0	2.0	142.48 (152)
A520	$0.53 \pm^{0.01}_{0.01}$	$496.00 \pm^{88.54}_{89.01}$	$11.08 \pm^{1.60}_{1.60}$	3.0	$7.38 \pm^{0.34}_{0.32}$	10.0	1.0	1.0	115.91 (129)
A586	$0.92 \pm^{0.16}_{0.12}$	$68.35 \pm^{18.96}_{15.05}$	$2.58 \pm^{0.43}_{0.39}$	$3.69 \pm^{0.29}_{0.40}$	$18.00 \pm^{3.99}_{2.39}$	$87.68 \pm^{18.20}_{11.86}$	$0.43 \pm^{0.06}_{0.06}$	2.0	44.07 (101)
A611	$1.28 \pm^{0.25}_{0.28}$	$37.50 \pm^{39.89}_{11.92}$	$4.56 \pm^{2.96}_{1.42}$	$2.76 \pm^{0.90}_{0.37}$	$14.42 \pm^{1.38}_{1.90}$	$36.59 \pm^{4.99}_{4.12}$	$0.47 \pm^{0.07}_{0.05}$	$2.38 \pm^{0.85}_{0.68}$	28.24 (44)
A665	$0.38 \pm^{0.06}_{0.03}$	$127.20 \pm^{29.24}_{35.58}$	$3.42 \pm^{0.68}_{0.45}$	$3.13 \pm^{0.29}_{0.31}$	$17.85 \pm^{1.31}_{1.67}$	60.0	$0.23 \pm^{0.07}_{0.04}$	1.0	238.30 (180)
A68	$1.14 \pm^{0.11}_{0.09}$	$225.90 \pm^{90.72}_{83.98}$	$3.52 \pm^{1.66}_{0.69}$	$5.35 \pm^{1.32}_{1.58}$	$13.05 \pm^{2.64}_{2.33}$	10.0	1.0	2.0	24.42 (80)
A697	$0.99 \pm^{0.19}_{0.19}$	$68.92 \pm^{18.88}_{12.28}$	$10.27 \pm^{4.59}_{4.10}$	$2.36 \pm^{0.28}_{0.12}$	$13.14 \pm^{2.52}_{1.78}$	100.0	$0.79 \pm^{0.13}_{0.15}$	2.0	31.15 (119)
A773	$1.33 \pm^{0.03}_{0.03}$	$56.17 \pm^{3.74}_{3.58}$	$7.11 \pm^{0.24}_{0.23}$	2.5	$9.58 \pm^{0.39}_{0.45}$	10.0	1.0	2.0	139.93 (94)
A781	$0.36 \pm^{0.02}_{0.02}$	$1442.00 \pm^{375.60}_{501.80}$	$33.81 \pm^{8.40}_{10.97}$	3.0	$6.18 \pm^{0.80}_{0.77}$	10.0	1.0	2.0	38.88 (74)
A963	$1.54 \pm^{0.19}_{0.14}$	$65.20 \pm^{13.01}_{16.06}$	$3.78 \pm^{1.09}_{0.58}$	$3.22 \pm^{0.35}_{0.42}$	$11.54 \pm^{1.04}_{1.27}$	$21.27 \pm^{3.08}_{3.15}$	$0.49 \pm^{0.04}_{0.04}$	2.0	82.70 (77)
MS 1455.0+2232	$3.27 \pm^{0.69}_{0.62}$	$7.45 \pm^{1.27}_{0.81}$	$3.19 \pm^{0.60}_{0.38}$	$2.68 \pm^{0.12}_{0.11}$	$15.79 \pm^{1.93}_{2.52}$	$40.92 \pm^{2.86}_{3.13}$	$0.31 \pm^{0.06}_{0.05}$	$2.10 \pm^{0.34}_{0.17}$	145.54 (100)
RX J0437.1+0043	$2.61 \pm^{0.31}_{0.30}$	$17.57 \pm^{2.43}_{2.08}$	$48.98 \pm^{14.49}_{21.81}$	$2.05 \pm^{0.04}_{0.01}$	$7.78 \pm^{0.56}_{0.42}$	$16.76 \pm^{2.65}_{2.61}$	$0.57 \pm^{0.06}_{0.06}$	2.0	57.38 (58)
RX J0439.0+0715	$0.72 \pm^{0.22}_{0.21}$	$288.90 \pm^{148.90}_{149.10}$	$2.45 \pm^{0.50}_{0.33}$	$7.47 \pm^{2.92}_{2.79}$	$17.08 \pm^{6.82}_{3.46}$	$41.93 \pm^{46.97}_{16.69}$	$0.16 \pm^{0.12}_{0.11}$	$1.04 \pm^{0.42}_{0.35}$	14.04 (89)
RX J1720.1+2638	$3.78 \pm^{0.29}_{0.23}$	$18.30 \pm^{1.28}_{1.66}$	$14.53 \pm^{2.39}_{1.66}$	$2.17 \pm^{0.02}_{0.03}$	$8.81 \pm^{0.49}_{0.38}$	$25.12 \pm^{1.46}_{1.28}$	$0.42 \pm^{0.03}_{0.03}$	$2.07 \pm^{0.19}_{0.18}$	172.51 (102)
RX J2129.6+0005	$1.99 \pm^{0.35}_{0.21}$	$25.84 \pm^{4.77}_{3.99}$	$4.39 \pm^{1.15}_{0.74}$	$2.66 \pm^{0.19}_{0.16}$	$13.81 \pm^{1.64}_{1.74}$	$23.23 \pm^{3.01}_{2.86}$	$0.25 \pm^{0.04}_{0.04}$	$1.48 \pm^{0.16}_{0.15}$	46.52 (75)
Z2089	$5.13 \pm^{1.20}_{1.09}$	$6.20 \pm^{3.94}_{2.13}$	$4.53 \pm^{1.63}_{1.16}$	$2.49 \pm^{0.22}_{0.15}$	$12.05 \pm^{2.75}_{2.65}$	$24.99 \pm^{33.15}_{10.42}$	0.2	$1.06 \pm^{0.40}_{0.32}$	6.72 (43)
Z3146	$5.22 \pm^{0.32}_{0.25}$	$19.25 \pm^{1.15}_{1.22}$	$13.31 \pm^{2.93}_{3.11}$	$2.23 \pm^{0.07}_{0.04}$	$8.88 \pm^{0.46}_{0.43}$	$15.88 \pm^{0.56}_{0.54}$	$0.47 \pm^{0.03}_{0.03}$	$3.30 \pm^{0.34}_{0.27}$	90.40 (90)
Z5247	$0.24 \pm^{0.01}_{0.01}$	$536.40 \pm^{26.68}_{25.53}$	10.0	3.0	$5.17 \pm^{0.43}_{0.39}$	10.0	1.0	2.0	35.03 (82)
Z5768	$0.49 \pm^{0.09}_{0.08}$	$82.87 \pm^{13.23}_{11.26}$	5.0	3.0	$4.82 \pm^{1.04}_{0.86}$	10.0	1.0	2.0	26.63 (60)
Z7215	$0.59 \pm^{0.14}_{0.15}$	$319.80 \pm^{121.60}_{119.70}$	$9.07 \pm^{4.53}_{3.42}$	$3.45 \pm^{0.96}_{0.65}$	$9.25 \pm^{2.33}_{1.70}$	$64.41 \pm^{35.54}_{40.99}$	$0.64 \pm^{0.18}_{0.14}$	2.0	17.64 (57)

Table 11. Cluster Masses

Cluster	Model	$\Delta = 2500$				$\Delta = 500$			
		r_Δ (arcsec)	$M_{\rm gas}$ (10^{13} $\mathrm{M}_\odot$)	$M_{\rm tot}$ (10^{14} $\mathrm{M}_\odot$)	$f_{\rm gas}$	r_Δ (arcsec)	$M_{\rm gas}$ (10^{13} $\mathrm{M}_\odot$)	$M_{\rm tot}$ (10^{14} $\mathrm{M}_\odot$)	$f_{\rm gas}$
A115									
	Vikh	$134.5 \pm^{13.7}_{12.7}$	$1.57 \pm^{0.28}_{0.25}$	$1.45 \pm^{0.49}_{0.37}$	$0.108 \pm^{0.015}_{0.013}$	$360.4 \pm^{21.4}_{19.2}$	$8.65 \pm^{0.84}_{0.71}$	$5.58 \pm^{1.06}_{0.84}$	$0.155 \pm^{0.013}_{0.012}$
	Poly	$139.7 \pm^{4.0}_{4.2}$	$1.68 \pm^{0.09}_{0.09}$	$1.62 \pm^{0.15}_{0.14}$	$0.103 \pm^{0.005}_{0.004}$	$318.7 \pm^{11.3}_{11.7}$	$7.08 \pm^{0.42}_{0.41}$	$3.86 \pm^{0.42}_{0.41}$	$0.184 \pm^{0.010}_{0.009}$
A1423									
	Vikh	$126.7 \pm^{7.0}_{7.8}$	$1.59 \pm^{0.15}_{0.16}$	$1.48 \pm^{0.26}_{0.25}$	$0.108 \pm^{0.009}_{0.007}$	$274.0 \pm^{18.8}_{16.8}$	$5.73 \pm^{0.58}_{0.49}$	$2.99 \pm^{0.66}_{0.52}$	$0.192 \pm^{0.020}_{0.019}$
	Poly	$130.8 \pm^{4.0}_{4.3}$	$1.69 \pm^{0.09}_{0.09}$	$1.63 \pm^{0.16}_{0.15}$	$0.104 \pm^{0.005}_{0.004}$	$267.3 \pm^{10.7}_{10.5}$	$5.49 \pm^{0.31}_{0.29}$	$2.78 \pm^{0.35}_{0.31}$	$0.198 \pm^{0.014}_{0.012}$
A1576									
	Vikh	$114.8 \pm^{8.5}_{9.8}$	$2.23 \pm^{0.28}_{0.29}$	$2.15 \pm^{0.52}_{0.50}$	$0.104 \pm^{0.014}_{0.010}$	$239.6 \pm^{20.2}_{22.0}$	$7.01 \pm^{0.78}_{0.79}$	$3.91 \pm^{1.07}_{0.98}$	$0.179 \pm^{0.033}_{0.024}$
	Poly	$114.5 \pm^{6.5}_{6.7}$	$2.28 \pm^{0.22}_{0.21}$	$2.14 \pm^{0.38}_{0.35}$	$0.107 \pm^{0.010}_{0.008}$	$242.5 \pm^{15.8}_{15.6}$	$7.26 \pm^{0.56}_{0.57}$	$4.05 \pm^{0.84}_{0.73}$	$0.179 \pm^{0.024}_{0.020}$
A1682									
	Vikh	$127.4 \pm^{10.1}_{11.0}$	$1.66 \pm^{0.26}_{0.27}$	$1.75 \pm^{0.45}_{0.42}$	$0.095 \pm^{0.010}_{0.008}$	$274.7 \pm^{24.0}_{23.0}$	$6.41 \pm^{0.74}_{0.71}$	$3.50 \pm^{1.00}_{0.81}$	$0.183 \pm^{0.029}_{0.024}$
	Poly	$122.0 \pm^{6.5}_{6.6}$	$1.54 \pm^{0.16}_{0.16}$	$1.53 \pm^{0.26}_{0.23}$	$0.101 \pm^{0.006}_{0.006}$	$299.4 \pm^{16.9}_{18.2}$	$7.18 \pm^{0.53}_{0.59}$	$4.53 \pm^{0.81}_{0.78}$	$0.159 \pm^{0.017}_{0.014}$
A1758									
	Vikh	$130.7 \pm^{20.3}_{22.5}$	$3.12 \pm^{0.96}_{0.96}$	$3.17 \pm^{1.72}_{1.37}$	$0.098 \pm^{0.022}_{0.015}$	$334.8 \pm^{39.9}_{42.6}$	$13.84 \pm^{2.25}_{2.22}$	$10.66 \pm^{4.28}_{3.57}$	$0.130 \pm^{0.034}_{0.023}$
	Poly	$130.3 \pm^{10.2}_{18.6}$	$3.09 \pm^{0.49}_{0.80}$	$3.14 \pm^{0.79}_{1.16}$	$0.098 \pm^{0.017}_{0.008}$	$370.1 \pm^{21.8}_{42.5}$	$14.84 \pm^{0.92}_{1.75}$	$14.41 \pm^{2.70}_{4.42}$	$0.104 \pm^{0.028}_{0.013}$
A1763									
	Vikh	$140.0 \pm^{8.9}_{9.0}$	$2.65 \pm^{0.31}_{0.28}$	$2.24 \pm^{0.46}_{0.40}$	$0.119 \pm^{0.011}_{0.009}$	$348.6 \pm^{25.3}_{24.7}$	$11.65 \pm^{1.12}_{1.10}$	$6.91 \pm^{1.61}_{1.37}$	$0.169 \pm^{0.022}_{0.019}$
	Poly	$139.7 \pm^{6.8}_{4.6}$	$2.68 \pm^{0.23}_{0.15}$	$2.22 \pm^{0.34}_{0.21}$	$0.120 \pm^{0.005}_{0.007}$	$330.0 \pm^{13.6}_{10.3}$	$10.72 \pm^{0.57}_{0.43}$	$5.86 \pm^{0.75}_{0.53}$	$0.183 \pm^{0.010}_{0.012}$
A1835									
	Vikh	$161.7 \pm^{6.5}_{7.2}$	$4.60 \pm^{0.23}_{0.25}$	$4.74 \pm^{0.60}_{0.61}$	$0.097 \pm^{0.008}_{0.007}$	$323.2 \pm^{8.6}_{8.6}$	$10.75 \pm^{0.28}_{0.29}$	$7.56 \pm^{0.62}_{0.59}$	$0.142 \pm^{0.008}_{0.007}$
	Poly	$143.8 \pm^{2.8}_{2.9}$	$4.00 \pm^{0.10}_{0.10}$	$3.33 \pm^{0.20}_{0.20}$	$0.120 \pm^{0.004}_{0.004}$	$309.6 \pm^{8.2}_{8.0}$	$10.36 \pm^{0.27}_{0.27}$	$6.65 \pm^{0.54}_{0.50}$	$0.156 \pm^{0.008}_{0.008}$
A1914									
	Vikh	$216.7 \pm^{7.5}_{7.5}$	$4.71 \pm^{0.21}_{0.21}$	$4.22 \pm^{0.45}_{0.42}$	$0.112 \pm^{0.007}_{0.007}$	$444.0 \pm^{23.2}_{25.6}$	$10.74 \pm^{0.56}_{0.61}$	$7.25 \pm^{1.20}_{1.19}$	$0.148 \pm^{0.019}_{0.015}$
	Poly	$219.4 \pm^{7.7}_{7.8}$	$4.82 \pm^{0.25}_{0.25}$	$4.37 \pm^{0.48}_{0.45}$	$0.110 \pm^{0.007}_{0.006}$	$487.5 \pm^{32.7}_{35.5}$	$11.30 \pm^{0.58}_{0.60}$	$9.59 \pm^{2.07}_{1.94}$	$0.118 \pm^{0.022}_{0.017}$
A2111									
	Vikh	$129.9 \pm^{10.8}_{8.7}$	$1.96 \pm^{0.28}_{0.23}$	$1.91 \pm^{0.51}_{0.36}$	$0.103 \pm^{0.009}_{0.010}$	$296.8 \pm^{19.5}_{17.0}$	$7.68 \pm^{0.69}_{0.62}$	$4.56 \pm^{0.96}_{0.74}$	$0.168 \pm^{0.017}_{0.017}$
	Poly	$121.1 \pm^{4.9}_{5.0}$	$1.74 \pm^{0.13}_{0.13}$	$1.55 \pm^{0.20}_{0.18}$	$0.112 \pm^{0.005}_{0.005}$	$305.3 \pm^{11.9}_{13.2}$	$8.04 \pm^{0.42}_{0.48}$	$4.96 \pm^{0.60}_{0.61}$	$0.162 \pm^{0.012}_{0.010}$
A2204									
	Vikh	$244.9 \pm^{6.1}_{6.0}$	$4.75 \pm^{0.15}_{0.15}$	$4.45 \pm^{0.34}_{0.32}$	$0.107 \pm^{0.005}_{0.004}$	$486.6 \pm^{16.2}_{15.6}$	$11.36 \pm^{0.41}_{0.39}$	$6.98 \pm^{0.72}_{0.65}$	$0.163 \pm^{0.010}_{0.010}$
	Poly	$233.7 \pm^{4.0}_{4.0}$	$4.50 \pm^{0.10}_{0.10}$	$3.87 \pm^{0.20}_{0.20}$	$0.116 \pm^{0.004}_{0.003}$	$496.3 \pm^{11.9}_{10.4}$	$11.58 \pm^{0.30}_{0.27}$	$7.40 \pm^{0.55}_{0.46}$	$0.156 \pm^{0.007}_{0.007}$
A2219									
	Vikh	$169.3 \pm^{6.4}_{6.6}$	$5.70 \pm^{0.39}_{0.39}$	$4.07 \pm^{0.48}_{0.46}$	$0.140 \pm^{0.007}_{0.007}$	$348.6 \pm^{18.0}_{18.6}$	$16.77 \pm^{1.17}_{1.17}$	$7.11 \pm^{1.16}_{1.08}$	$0.236 \pm^{0.023}_{0.019}$
	Poly	$166.2 \pm^{5.0}_{5.3}$	$5.52 \pm^{0.32}_{0.32}$	$3.85 \pm^{0.36}_{0.35}$	$0.143 \pm^{0.006}_{0.005}$	$369.6 \pm^{16.8}_{16.6}$	$18.21 \pm^{1.02}_{1.00}$	$8.48 \pm^{1.21}_{1.09}$	$0.215 \pm^{0.018}_{0.017}$
A2261									
	Vikh	$154.5 \pm^{7.7}_{6.7}$	$3.63 \pm^{0.25}_{0.21}$	$3.04 \pm^{0.48}_{0.38}$	$0.119 \pm^{0.009}_{0.009}$	$319.3 \pm^{18.8}_{23.4}$	$9.79 \pm^{0.65}_{0.79}$	$5.37 \pm^{1.01}_{1.10}$	$0.182 \pm^{0.028}_{0.019}$
	Poly	$144.4 \pm^{5.4}_{5.3}$	$3.32 \pm^{0.17}_{0.16}$	$2.48 \pm^{0.29}_{0.26}$	$0.134 \pm^{0.008}_{0.008}$	$308.0 \pm^{13.7}_{14.4}$	$9.37 \pm^{0.48}_{0.50}$	$4.82 \pm^{0.67}_{0.65}$	$0.194 \pm^{0.018}_{0.015}$
A2390									
	Vikh	$188.7 \pm^{12.1}_{11.8}$	$5.71 \pm^{0.57}_{0.54}$	$6.11 \pm^{1.25}_{1.07}$	$0.093 \pm^{0.009}_{0.008}$	$387.7 \pm^{34.0}_{35.3}$	$13.84 \pm^{1.21}_{1.24}$	$10.60 \pm^{3.04}_{2.64}$	$0.131 \pm^{0.028}_{0.020}$
	Poly	$180.2 \pm^{7.2}_{7.3}$	$5.33 \pm^{0.35}_{0.33}$	$5.32 \pm^{0.66}_{0.62}$	$0.100 \pm^{0.006}_{0.006}$	$372.0 \pm^{24.6}_{21.6}$	$13.33 \pm^{0.84}_{0.76}$	$9.36 \pm^{1.98}_{1.54}$	$0.142 \pm^{0.018}_{0.018}$
A2552									
	Vikh	$115.9 \pm^{8.1}_{9.5}$	$3.05 \pm^{0.35}_{0.39}$	$2.67 \pm^{0.60}_{0.60}$	$0.114 \pm^{0.014}_{0.011}$	$247.2 \pm^{13.7}_{16.4}$	$9.66 \pm^{0.70}_{0.81}$	$5.19 \pm^{0.91}_{0.96}$	$0.186 \pm^{0.023}_{0.017}$
	Poly	$109.5 \pm^{4.6}_{6.0}$	$2.80 \pm^{0.19}_{0.25}$	$2.25 \pm^{0.29}_{0.35}$	$0.124 \pm^{0.010}_{0.007}$	$254.2 \pm^{10.2}_{13.3}$	$9.97 \pm^{0.53}_{0.66}$	$5.64 \pm^{0.71}_{0.84}$	$0.177 \pm^{0.017}_{0.012}$
A2631									
	Vikh	$117.7 \pm^{7.5}_{8.7}$	$2.87 \pm^{0.33}_{0.36}$	$2.30 \pm^{0.47}_{0.47}$	$0.125 \pm^{0.012}_{0.009}$	$273.4 \pm^{17.9}_{20.3}$	$10.13 \pm^{0.67}_{0.78}$	$5.75 \pm^{1.21}_{1.18}$	$0.176 \pm^{0.029}_{0.021}$
	Poly	$117.4 \pm^{6.5}_{6.7}$	$2.87 \pm^{0.28}_{0.29}$	$2.28 \pm^{0.40}_{0.37}$	$0.126 \pm^{0.009}_{0.008}$	$282.0 \pm^{21.2}_{17.8}$	$10.50 \pm^{0.67}_{0.62}$	$6.31 \pm^{1.54}_{1.12}$	$0.166 \pm^{0.024}_{0.024}$
A267									
	Vikh	$115.4 \pm^{9.3}_{10.4}$	$1.61 \pm^{0.19}_{0.19}$	$1.37 \pm^{0.36}_{0.34}$	$0.117 \pm^{0.020}_{0.014}$	$251.5 \pm^{16.9}_{18.6}$	$4.82 \pm^{0.33}_{0.34}$	$2.83 \pm^{0.61}_{0.58}$	$0.170 \pm^{0.029}_{0.021}$
	Poly	$108.5 \pm^{4.3}_{4.7}$	$1.49 \pm^{0.09}_{0.10}$	$1.14 \pm^{0.14}_{0.14}$	$0.131 \pm^{0.009}_{0.008}$	$224.3 \pm^{13.9}_{13.5}$	$4.36 \pm^{0.27}_{0.27}$	$2.01 \pm^{0.40}_{0.34}$	$0.217 \pm^{0.029}_{0.025}$
A520									
	Vikh	$166.5 \pm^{6.0}_{7.2}$	$3.16 \pm^{0.22}_{0.25}$	$2.82 \pm^{0.31}_{0.35}$	$0.112 \pm^{0.006}_{0.005}$	$367.1 \pm^{9.3}_{9.2}$	$10.71 \pm^{0.30}_{0.29}$	$6.04 \pm^{0.47}_{0.44}$	$0.177 \pm^{0.009}_{0.009}$
	Poly	$128.9 \pm^{4.3}_{4.4}$	$1.83 \pm^{0.12}_{0.13}$	$1.31 \pm^{0.13}_{0.13}$	$0.140 \pm^{0.005}_{0.005}$	$393.9 \pm^{11.7}_{12.0}$	$11.90 \pm^{0.36}_{0.39}$	$7.47 \pm^{0.69}_{0.66}$	$0.159 \pm^{0.010}_{0.009}$
A586									
	Vikh	$176.8 \pm^{4.0}_{4.2}$	$2.26 \pm^{0.06}_{0.07}$	$2.28 \pm^{0.16}_{0.16}$	$0.099 \pm^{0.004}_{0.004}$	$354.3 \pm^{17.3}_{19.4}$	$5.69 \pm^{0.29}_{0.33}$	$3.67 \pm^{0.56}_{0.57}$	$0.155 \pm^{0.018}_{0.014}$
	Poly	$177.9 \pm^{5.5}_{5.8}$	$2.30 \pm^{0.09}_{0.09}$	$2.32 \pm^{0.22}_{0.22}$	$0.099 \pm^{0.006}_{0.005}$	$357.1 \pm^{14.7}_{15.7}$	$5.66 \pm^{0.24}_{0.24}$	$3.76 \pm^{0.48}_{0.47}$	$0.151 \pm^{0.014}_{0.012}$
A611									
	Vikh	$125.3 \pm^{8.3}_{10.1}$	$2.79 \pm^{0.26}_{0.29}$	$3.02 \pm^{0.64}_{0.67}$	$0.092 \pm^{0.014}_{0.009}$	$285.3 \pm^{22.2}_{20.9}$	$8.36 \pm^{0.52}_{0.60}$	$7.13 \pm^{1.80}_{1.45}$	$0.118 \pm^{0.019}_{0.019}$
	Poly	$124.9 \pm^{8.2}_{7.4}$	$2.81 \pm^{0.25}_{0.22}$	$2.99 \pm^{0.63}_{0.50}$	$0.094 \pm^{0.010}_{0.010}$	$269.3 \pm^{27.0}_{28.0}$	$7.71 \pm^{0.73}_{0.83}$	$6.00 \pm^{1.99}_{1.69}$	$0.128 \pm^{0.032}_{0.023}$
A665									
	Vikh	$166.4 \pm^{11.5}_{8.0}$	$2.22 \pm^{0.29}_{0.19}$	$2.23 \pm^{0.50}_{0.31}$	$0.100 \pm^{0.006}_{0.008}$	$464.9 \pm^{29.8}_{33.6}$	$11.82 \pm^{0.87}_{1.02}$	$9.74 \pm^{1.99}_{1.96}$	$0.121 \pm^{0.017}_{0.013}$
	Poly	$178.5 \pm^{5.1}_{6.2}$	$2.56 \pm^{0.13}_{0.16}$	$2.76 \pm^{0.24}_{0.28}$	$0.093 \pm^{0.004}_{0.003}$	$412.7 \pm^{16.9}_{15.6}$	$9.87 \pm^{0.55}_{0.51}$	$6.81 \pm^{0.87}_{0.74}$	$0.145 \pm^{0.009}_{0.009}$
A68									
	Vikh	$137.7 \pm^{10.7}_{12.0}$	$3.09 \pm^{0.36}_{0.39}$	$2.96 \pm^{0.75}_{0.71}$	$0.105 \pm^{0.016}_{0.012}$	$305.3 \pm^{38.0}_{33.8}$	$8.31 \pm^{0.83}_{0.81}$	$6.46 \pm^{2.73}_{1.91}$	$0.129 \pm^{0.037}_{0.031}$
	Poly	$141.2 \pm^{8.6}_{8.6}$	$3.24 \pm^{0.30}_{0.30}$	$3.20 \pm^{0.62}_{0.55}$	$0.101 \pm^{0.010}_{0.009}$	$290.5 \pm^{32.1}_{25.3}$	$7.92 \pm^{0.60}_{0.55}$	$5.57 \pm^{2.06}_{1.33}$	$0.143 \pm^{0.032}_{0.032}$
A697									
	Vikh	$135.3 \pm^{10.4}_{11.1}$	$4.58 \pm^{0.59}_{0.62}$	$3.61 \pm^{0.90}_{0.82}$	$0.127 \pm^{0.015}_{0.013}$	$309.9 \pm^{26.5}_{30.2}$	$15.48 \pm^{1.68}_{1.83}$	$8.68 \pm^{2.43}_{2.30}$	$0.178 \pm^{0.035}_{0.024}$
	Poly	$130.7 \pm^{6.7}_{7.8}$	$4.32 \pm^{0.38}_{0.44}$	$3.26 \pm^{0.53}_{0.55}$	$0.133 \pm^{0.011}_{0.009}$	$326.8 \pm^{20.4}_{18.3}$	$16.60 \pm^{1.22}_{1.12}$	$10.18 \pm^{2.03}_{1.62}$	$0.163 \pm^{0.019}_{0.018}$
A773									
	Vikh	$144.0 \pm^{7.5}_{6.7}$	$2.71 \pm^{0.20}_{0.19}$	$2.27 \pm^{0.38}_{0.30}$	$0.119 \pm^{0.009}_{0.009}$	$319.8 \pm^{14.8}_{13.4}$	$8.60 \pm^{0.48}_{0.44}$	$4.98 \pm^{0.73}_{0.60}$	$0.173 \pm^{0.014}_{0.014}$
	Poly	$146.1 \pm^{3.0}_{3.6}$	$2.80 \pm^{0.09}_{0.11}$	$2.38 \pm^{0.15}_{0.17}$	$0.118 \pm^{0.004}_{0.004}$	$334.0 \pm^{6.6}_{7.7}$	$9.13 \pm^{0.19}_{0.23}$	$5.67 \pm^{0.35}_{0.38}$	$0.161 \pm^{0.007}_{0.006}$
A781									
	Vikh	$69.7 \pm^{18.2}_{21.7}$	$0.71 \pm^{0.54}_{0.44}$	$0.57 \pm^{0.57}_{0.38}$	$0.126 \pm^{0.020}_{0.016}$	$249.0 \pm^{22.7}_{25.0}$	$8.50 \pm^{0.90}_{0.98}$	$5.16 \pm^{1.55}_{1.40}$	$0.165 \pm^{0.036}_{0.025}$
	Poly	$68.4 \pm^{8.8}_{8.5}$	$0.68 \pm^{0.23}_{0.19}$	$0.53 \pm^{0.23}_{0.18}$	$0.127 \pm^{0.011}_{0.010}$	$280.4 \pm^{32.0}_{30.0}$	$9.95 \pm^{1.11}_{1.16}$	$7.37 \pm^{2.82}_{2.13}$	$0.135 \pm^{0.033}_{0.027}$
A963									
	Vikh	$153.8 \pm^{8.2}_{9.4}$	$2.66 \pm^{0.20}_{0.23}$	$2.43 \pm^{0.41}_{0.42}$	$0.110 \pm^{0.012}_{0.009}$	$308.2 \pm^{18.9}_{24.1}$	$6.49 \pm^{0.34}_{0.46}$	$3.91 \pm^{0.76}_{0.85}$	$0.166 \pm^{0.031}_{0.021}$
	Poly	$149.9 \pm^{5.0}_{5.3}$	$2.55 \pm^{0.12}_{0.12}$	$2.25 \pm^{0.23}_{0.23}$	$0.114 \pm^{0.007}_{0.006}$	$309.5 \pm^{17.7}_{16.3}$	$6.57 \pm^{0.35}_{0.34}$	$3.96 \pm^{0.72}_{0.59}$	$0.166 \pm^{0.019}_{0.019}$

Continued on next page...

Table 11. Cluster Masses–Continued

		Δ = 2500				Δ = 500			
Cluster	Model	r_Δ (arcsec)	$M_{\rm gas}$ (10^{13} M$_\odot$)	$M_{\rm tot}$ (10^{14} M$_\odot$)	$f_{\rm gas}$	r_Δ (arcsec)	$M_{\rm gas}$ (10^{13} M$_\odot$)	$M_{\rm tot}$ (10^{14} M$_\odot$)	$f_{\rm gas}$
<u>M1455</u>									
	Vikh	$104.9 \pm^{3.7}_{4.2}$	$1.69 \pm^{0.07}_{0.08}$	$1.35 \pm^{0.15}_{0.15}$	$0.125 \pm^{0.010}_{0.008}$	$236.8 \pm^{9.0}_{10.1}$	$4.64 \pm^{0.18}_{0.21}$	$3.11 \pm^{0.37}_{0.38}$	$0.149 \pm^{0.013}_{0.011}$
	Poly	$105.3 \pm^{2.5}_{2.0}$	$1.70 \pm^{0.04}_{0.03}$	$1.37 \pm^{0.10}_{0.08}$	$0.124 \pm^{0.005}_{0.005}$	$212.9 \pm^{6.6}_{5.0}$	$4.24 \pm^{0.12}_{0.09}$	$2.26 \pm^{0.22}_{0.16}$	$0.187 \pm^{0.009}_{0.011}$
<u>R0437</u>									
	Vikh	$124.1 \pm^{7.9}_{8.1}$	$2.80 \pm^{0.25}_{0.25}$	$2.86 \pm^{0.58}_{0.52}$	$0.098 \pm^{0.011}_{0.009}$	$262.9 \pm^{24.7}_{25.6}$	$7.59 \pm^{0.81}_{0.76}$	$5.44 \pm^{1.68}_{1.44}$	$0.140 \pm^{0.031}_{0.022}$
	Poly	$116.8 \pm^{3.8}_{3.5}$	$2.59 \pm^{0.12}_{0.11}$	$2.38 \pm^{0.24}_{0.21}$	$0.108 \pm^{0.006}_{0.005}$	$279.8 \pm^{10.6}_{10.1}$	$8.01 \pm^{0.32}_{0.30}$	$6.55 \pm^{0.77}_{0.68}$	$0.122 \pm^{0.010}_{0.009}$
<u>R0439</u>									
	Vikh	$146.4 \pm^{8.5}_{8.6}$	$2.94 \pm^{0.24}_{0.25}$	$2.77 \pm^{0.51}_{0.46}$	$0.106 \pm^{0.011}_{0.009}$	$285.1 \pm^{23.0}_{24.4}$	$6.95 \pm^{0.50}_{0.55}$	$4.09 \pm^{1.07}_{0.96}$	$0.170 \pm^{0.035}_{0.026}$
	Poly	$138.3 \pm^{5.8}_{5.8}$	$2.72 \pm^{0.17}_{0.17}$	$2.33 \pm^{0.30}_{0.28}$	$0.117 \pm^{0.008}_{0.008}$	$278.6 \pm^{18.8}_{17.0}$	$6.80 \pm^{0.40}_{0.40}$	$3.81 \pm^{0.82}_{0.65}$	$0.178 \pm^{0.025}_{0.024}$
<u>R1720</u>									
	Vikh	$213.3 \pm^{11.2}_{7.2}$	$3.31 \pm^{0.23}_{0.15}$	$3.59 \pm^{0.60}_{0.35}$	$0.092 \pm^{0.005}_{0.008}$	$442.5 \pm^{41.0}_{22.2}$	$8.23 \pm^{0.86}_{0.44}$	$6.41 \pm^{1.95}_{0.92}$	$0.128 \pm^{0.014}_{0.020}$
	Poly	$189.1 \pm^{5.4}_{5.1}$	$2.84 \pm^{0.11}_{0.09}$	$2.50 \pm^{0.22}_{0.20}$	$0.113 \pm^{0.006}_{0.005}$	$427.7 \pm^{12.5}_{12.8}$	$7.91 \pm^{0.22}_{0.21}$	$5.79 \pm^{0.52}_{0.51}$	$0.137 \pm^{0.009}_{0.008}$
<u>R2129</u>									
	Vikh	$143.9 \pm^{8.1}_{7.5}$	$3.02 \pm^{0.23}_{0.21}$	$2.78 \pm^{0.49}_{0.41}$	$0.109 \pm^{0.010}_{0.010}$	$283.9 \pm^{21.0}_{18.1}$	$7.41 \pm^{0.58}_{0.51}$	$4.26 \pm^{1.02}_{0.76}$	$0.174 \pm^{0.024}_{0.023}$
	Poly	$138.4 \pm^{4.8}_{4.9}$	$2.87 \pm^{0.13}_{0.13}$	$2.46 \pm^{0.27}_{0.25}$	$0.116 \pm^{0.007}_{0.007}$	$292.4 \pm^{13.6}_{14.1}$	$7.66 \pm^{0.38}_{0.38}$	$4.65 \pm^{0.68}_{0.64}$	$0.165 \pm^{0.017}_{0.014}$
<u>Z2089</u>									
	Vikh	$91.1 \pm^{5.6}_{5.4}$	$1.54 \pm^{0.12}_{0.11}$	$1.07 \pm^{0.21}_{0.18}$	$0.143 \pm^{0.017}_{0.014}$	$211.0 \pm^{14.7}_{16.9}$	$4.38 \pm^{0.31}_{0.33}$	$2.67 \pm^{0.60}_{0.59}$	$0.165 \pm^{0.032}_{0.023}$
	Poly	$107.7 \pm^{4.2}_{4.2}$	$1.40 \pm^{0.07}_{0.06}$	$1.16 \pm^{0.14}_{0.13}$	$0.121 \pm^{0.010}_{0.009}$	$225.9 \pm^{12.1}_{14.1}$	$3.48 \pm^{0.19}_{0.20}$	$2.14 \pm^{0.36}_{0.38}$	$0.163 \pm^{0.024}_{0.018}$
<u>Z3146</u>									
	Vikh	$132.8 \pm^{8.5}_{8.0}$	$4.82 \pm^{0.37}_{0.36}$	$3.68 \pm^{0.75}_{0.63}$	$0.131 \pm^{0.015}_{0.014}$	$277.2 \pm^{20.9}_{23.1}$	$10.96 \pm^{0.70}_{0.78}$	$6.69 \pm^{1.62}_{1.54}$	$0.164 \pm^{0.034}_{0.024}$
	Poly	$120.5 \pm^{3.4}_{3.6}$	$4.29 \pm^{0.15}_{0.15}$	$2.75 \pm^{0.24}_{0.24}$	$0.156 \pm^{0.009}_{0.008}$	$273.6 \pm^{9.8}_{10.8}$	$10.79 \pm^{0.32}_{0.34}$	$6.42 \pm^{0.72}_{0.73}$	$0.168 \pm^{0.016}_{0.013}$
<u>Z5247</u>									
	Vikh	$91.9 \pm^{10.3}_{13.5}$	$0.61 \pm^{0.18}_{0.20}$	$0.69 \pm^{0.25}_{0.26}$	$0.089 \pm^{0.009}_{0.006}$	$222.0 \pm^{11.5}_{13.5}$	$4.14 \pm^{0.36}_{0.40}$	$1.93 \pm^{0.32}_{0.33}$	$0.215 \pm^{0.021}_{0.016}$
	Poly	$74.6 \pm^{6.0}_{5.4}$	$0.36 \pm^{0.08}_{0.06}$	$0.37 \pm^{0.09}_{0.07}$	$0.099 \pm^{0.004}_{0.004}$	$255.2 \pm^{14.0}_{13.3}$	$5.56 \pm^{0.46}_{0.45}$	$2.93 \pm^{0.51}_{0.43}$	$0.190 \pm^{0.016}_{0.016}$
<u>Z5768</u>									
	Vikh	$81.4 \pm^{10.3}_{11.7}$	$0.47 \pm^{0.10}_{0.10}$	$0.68 \pm^{0.29}_{0.25}$	$0.069 \pm^{0.018}_{0.012}$	$178.1 \pm^{21.0}_{24.0}$	$1.85 \pm^{0.30}_{0.33}$	$1.43 \pm^{0.57}_{0.50}$	$0.131 \pm^{0.036}_{0.025}$
	Poly	$80.6 \pm^{10.6}_{9.4}$	$0.54 \pm^{0.12}_{0.11}$	$0.66 \pm^{0.30}_{0.21}$	$0.080 \pm^{0.014}_{0.012}$	$191.8 \pm^{18.9}_{17.9}$	$2.26 \pm^{0.27}_{0.28}$	$1.78 \pm^{0.58}_{0.45}$	$0.128 \pm^{0.029}_{0.025}$
<u>Z7215</u>									
	Vikh	$128.6 \pm^{16.2}_{15.9}$	$2.72 \pm^{0.51}_{0.48}$	$3.31 \pm^{1.41}_{1.08}$	$0.082 \pm^{0.019}_{0.014}$	$273.7 \pm^{25.6}_{25.0}$	$7.10 \pm^{0.66}_{0.59}$	$6.39 \pm^{1.96}_{1.60}$	$0.112 \pm^{0.027}_{0.021}$
	Poly	$114.5 \pm^{13.1}_{12.4}$	$2.30 \pm^{0.41}_{0.37}$	$2.34 \pm^{0.89}_{0.68}$	$0.098 \pm^{0.019}_{0.015}$	$319.0 \pm^{44.8}_{45.0}$	$7.80 \pm^{0.88}_{0.76}$	$10.11 \pm^{4.88}_{3.70}$	$0.078 \pm^{0.034}_{0.023}$

Appendices

A APPENDIX: MODEL FITS TO TEMPERATURE PROFILES

Temperature profiles for all the clusters with the Vikhlinin et al. (2006) model (blue) and the Bulbul et al. (2010) model (red) are shown in Figure 12. Table 13 shows the radius out to which the temperature was measured and the estimated r_{500} value for each cluster. Out of the 7 clusters, 5 clusters have temperature profiles which extended to $\geqslant$ 85% of r_{500}. The temperature profiles of *Abell 1758* and *Abell 611* only reached 73% and 63% of r_{500}, respectively. Both of these clusters suffered from solar flares, which did not allow the determination of the temperature profile out to r_{500}. The effects of extrapolating the temperature profiles for these 7 clusters are not believed to significantly affect mass measurements.

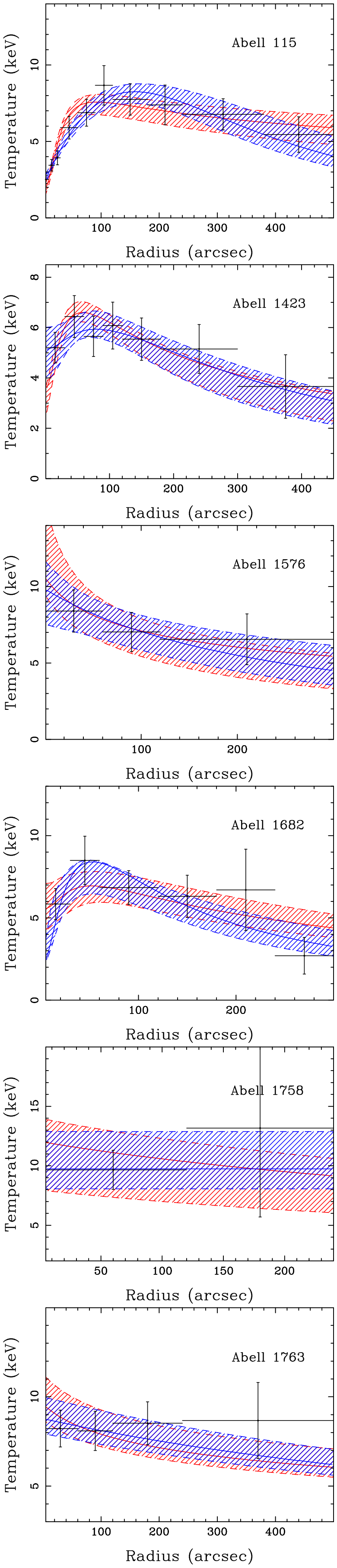

REFERENCES

Afshordi N., Lin Y.-T., Nagai D., Sanderson A. J. R., 2007, MNRAS, 378, 293

Allen S. W., Rapetti D. A., Schmidt R. W., Ebeling H., Morris R. G., Fabian A. C., 2008, MNRAS, 383, 879

Allen S. W., Schmidt R. W., Ebeling H., Fabian A. C., van Speybroeck L., 2004, MNRAS, 353, 457

Allen S. W., Schmidt R. W., Fabian A. C., 2002, MNRAS, 335, 256

Arnaud K. A., 1996, in Astronomical Society of the Pacific Conference Series, Vol. 101, Astronomical Data Analysis Software and Systems V, Jacoby G. H., Barnes J., eds., p. 17

Arnaud M., Pointecouteau E., Pratt G. W., 2007, Astronomy and Astrophysics, 474, L37

Bialek J. J., Evrard A. E., Mohr J. J., 2001, Astrophysical Journal, 555, 597

Bode P., Ostriker J. P., Vikhlinin A., 2009, Astrophysical Journal, 700, 989

Bonamente M., Joy M. K., Carlstrom J. E., Reese E. D., LaRoque S. J., 2004, Astrophysical Journal, 614, 56

Bonamente M., Joy M. K., LaRoque S. J., Carlstrom J. E., Reese E. D., Dawson K. S., 2006, Astrophysical Journal, 647, 25

Bonamente M., Landry D., Maughan B., Giles P., Joy M., Nevalainen J., 2012, ArXiv e-prints

Briel U. G., Henry J. P., Boehringer H., 1992, Astronomy and Astrophysics, 259, L31

Bulbul G. E., Hasler N., Bonamente M., Joy M., 2010, Astrophysical Journal, 720, 1038

Carroll S. M., Press W. H., Turner E. L., 1992, Annu. Rev. Astron. Astrophys., 30, 499

Cavaliere A., Lapi A., 2008, Astrophysical Journal, Letters, 673, L5

Dahle H., 2006, Astrophysical Journal, 653, 954

David L. P., Jones C., Forman W., 1995, Astrophysical Journal, 445, 578

Ebeling H., Edge A. C., Allen S. W., Crawford C. S., Fabian A. C., Huchra J. P., 2000, MNRAS, 318, 333

Table 13. Extrapolation of Temperature Profiles out to r_{500}

Cluster	Max Radius of $T(r)$ (arcsec)	r_{500} (arcsec)	Per cent of r_{500} (%)
A1758	240	330	73
A1914	420	440	95
A611	180	285	63
RX J0437.1+0043	240	260	92
RX J1720.1+2638	400	440	91
Z2089	180	210	86
Z7215	240	275	87

Ebeling H., Edge A. C., Bohringer H., Allen S. W., Crawford C. S., Fabian A. C., Voges W., Huchra J. P., 1998, MNRAS, 301, 881

Eckert D. et al., 2012, Astronomy and Astrophysics, 541, A57

Ettori S., Fabian A. C., 1999, MNRAS, 305, 834

Ettori S., Morandi A., Tozzi P., Balestra I., Borgani S., Rosati P., Lovisari L., Terenziani F., 2009, Astronomy and Astrophysics, 501, 61

Evrard A. E., 1997, MNRAS, 292, 289

Fabian A. C., 1991, MNRAS, 253, 29P

Giles P. A., Maughan B. J., Dahle H., Bonamente M., Jones C., Joy M., Landry D., Murray S., 2012, in prep

Giodini S. et al., 2009, Astrophysical Journal, 703, 982

Gonzalez A. H., Zaritsky D., Zabludoff A. I., 2007, Astrophysical Journal, 666, 147

Govoni F., Markevitch M., Vikhlinin A., van Speybroeck L., Feretti L., Giovannini G., 2004, Astrophysical Journal, 605, 695

Grego L., Carlstrom J., Reese E., Holder G., Holzapfel W., Joy M., Mohr J., Patel S., 2001, Astrophysical Journal, 552, 2

Hasler N. et al., 2012, Astrophysical Journal, 748, 113

Hickox R. C., Markevitch M., 2006, Astrophysical Journal, 645, 95

Hudson D. S., Mittal R., Reiprich T. H., Nulsen P. E. J., Andernach H., Sarazin C. L., 2010, Astronomy and Astrophysics, 513, A37

Kalberla P. M. W., Burton W. B., Hartmann D., Arnal E. M., Bajaja E., Morras R., Pöppel W. G. L., 2005, Astronomy and Astrophysics, 440, 775

Komatsu E. et al., 2011, Astrophysical Journal, Supplement, 192, 18

LaRoque S. J., Bonamente M., Carlstrom J. E., Joy M. K., Nagai D., Reese E. D., Dawson K. S., 2006, Astrophysical Journal, 652, 917

Lau E. T., Kravtsov A. V., Nagai D., 2009, Astrophysical Journal, 705, 1129

Lin Y.-T., Mohr J. J., Stanford S. A., 2003, Astrophysical Journal, 591, 749

Mantz A., Allen S. W., 2011, ArXiv e-prints

Markevitch M. et al., 2003, Astrophysical Journal, 583, 70

Mathiesen B., Evrard A. E., Mohr J. J., 1999, Astrophysical Journal, Letters, 520, L21

McCarthy I. G., Bower R. G., Balogh M. L., 2007, MNRAS, 377, 1457

Metzler C. A., Evrard A. E., 1994, Astrophysical Journal, 437, 564

Miller E. D., Bautz M., George J., Mushotzky R., Davis D., Henry J. P., 2012, in American Institute of Physics Conference Series, Vol. 1427, American Institute of Physics Conference Series, Petre R., Mitsuda K., Angelini L., eds., pp. 13–20

Mohr J. J., Mathiesen B., Evrard A. E., 1999, Astrophysical Journal, 517, 627

Nagai D., Lau E. T., 2011, Astrophysical Journal, Letters, 731, L10

Nagai D., Vikhlinin A., Kravtsov A. V., 2007, Astrophysical Journal, 655, 98

Pen U.-L., 1997, New Astron., 2, 309

Pointecouteau E., Arnaud M., Pratt G. W., 2005, Astronomy and Astrophysics, 435, 1

Poole G. B., Fardal M. A., Babul A., McCarthy I. G., Quinn T., Wadsley J., 2006, MNRAS, 373, 881

Press W. H., Schechter P., 1974, Astrophysical Journal, 187, 425

Rasheed B., Bahcall N., Bode P., 2010, ArXiv e-prints

Sarazin C. L., 1988, X-ray Emission From Clusters of Galaxies. Cambridge University Press

Simionescu A. et al., 2011, Science, 331, 1576

Smith R. K., Brickhouse N. S., Liedahl D. A., Raymond J. C., 2001, Astrophysical Journal, Letters, 556, L91

Snowden S. L. et al., 1997, Astrophysical Journal, 485, 125

Sun M., Voit G. M., Donahue M., Jones C., Forman W., Vikhlinin A., 2009, Astrophysical Journal, 693, 1142

Takei Y. et al., 2008, Astrophysical Journal, 680, 1049

Takizawa M., Mineshige S., 1998, Astrophysical Journal, 499, 82

Umetsu K. et al., 2009, Astrophysical Journal, 694, 1643

Valdarnini R., 2003, MNRAS, 339, 1117

Vikhlinin A., Burenin R., Forman W. R., Jones C., Hornstrup A., Murray S. S., Quintana H., 2007, in Heating versus Cooling in Galaxies and Clusters of Galaxies, Böhringer H., Pratt G. W., Finoguenov A., Schuecker P., eds., p. 48

Vikhlinin A., Kravtsov A., Forman W., Jones C., Markevitch M., Murray S. S., Van Speybroeck L., 2006, Astrophysical Journal, 640, 691

White D. A., Fabian A. C., 1995, MNRAS, 273, 72

White S. D. M., Frenk C. S., 1991, Astrophysical Journal, 379, 52

White S. D. M., Navarro J. F., Evrard A. E., Frenk C. S., 1993, Nature, 366, 429

White S. D. M., Rees M. J., 1978, MNRAS, 183, 341

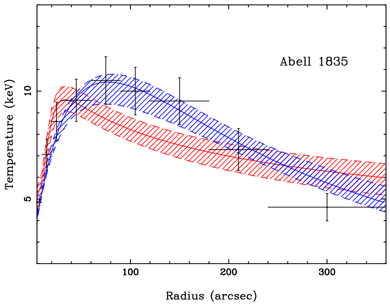
Abell 1835
Temperature (keV)
5
10
100
200
300
Radius (arcsec)

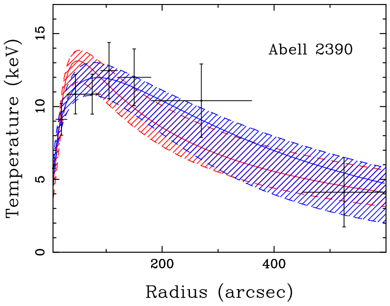
Abell 2390
Temperature (keV)
0
5
10
15
200
400
Radius (arcsec)

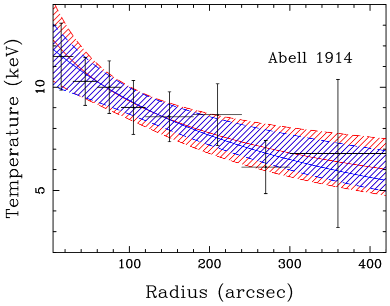
Abell 1914
Temperature (keV)
5
10
100
200
300
400
Radius (arcsec)

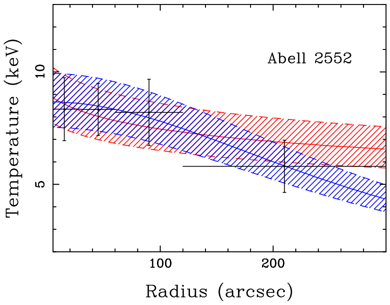
Abell 2552
Temperature (keV)
5
10
100
200
Radius (arcsec)

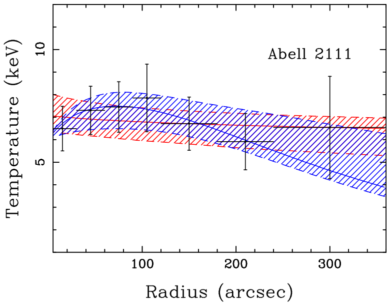
Abell 2111
Temperature (keV)
5
10
100
200
300
Radius (arcsec)

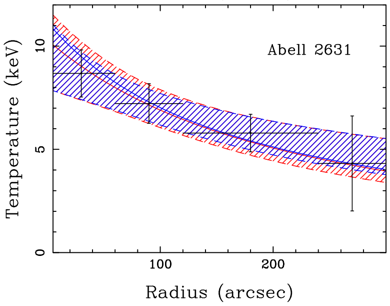
Abell 2631
Temperature (keV)
0
5
10
100
200
Radius (arcsec)

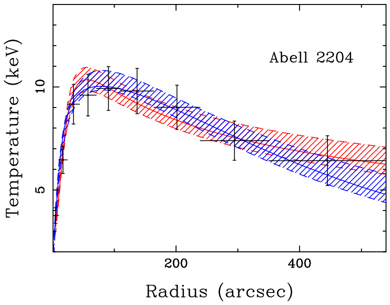
Abell 2204
Temperature (keV)
5
10
200
400
Radius (arcsec)

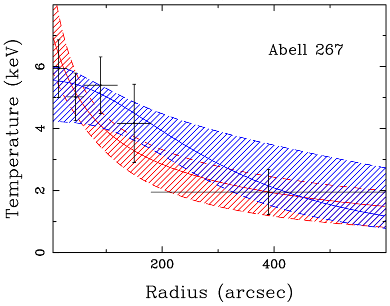
Abell 267
Temperature (keV)
0
2
4
6
200
400
Radius (arcsec)

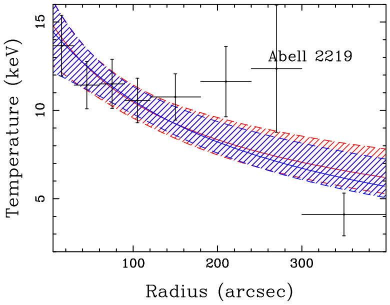
Abell 2219
Temperature (keV)
5
10
15
100
200
300
Radius (arcsec)

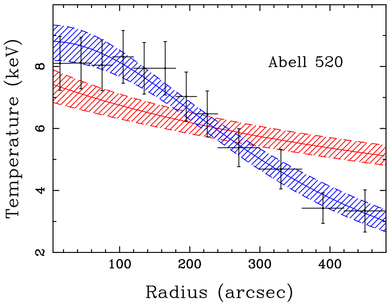
Abell 520
Temperature (keV)
2
4
6
8
100
200
300
400
Radius (arcsec)

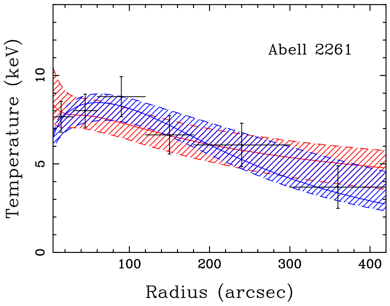
Abell 2261
Temperature (keV)
0
5
10
100
200
300
400
Radius (arcsec)

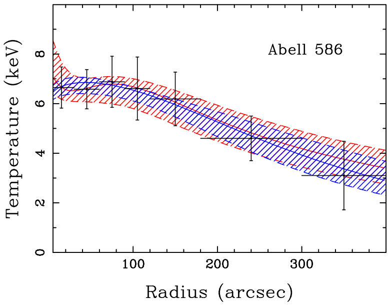
Abell 586
Temperature (keV)
0
2
4
6
8
100
200
300
Radius (arcsec)

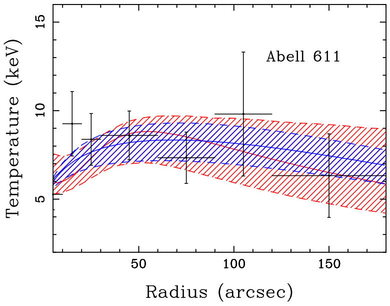
Abell 611
Temperature (keV)
5
10
15
50
100
150
Radius (arcsec)

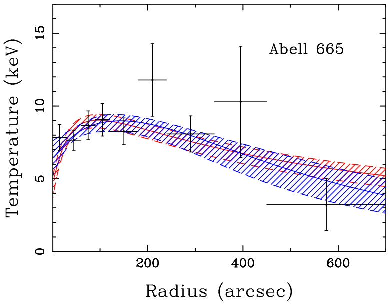
Abell 665
Temperature (keV)
0
5
10
15
200
400
600
Radius (arcsec)

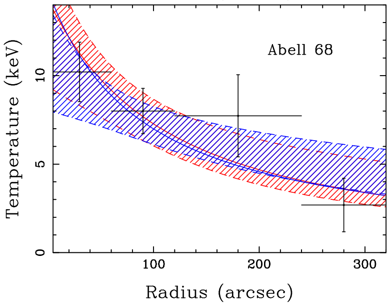
Abell 68
Temperature (keV)
0
5
10
100
200
300
Radius (arcsec)

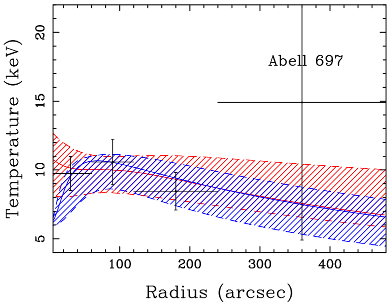
Abell 697
Temperature (keV)
5
10
15
20
100
200
300
400
Radius (arcsec)

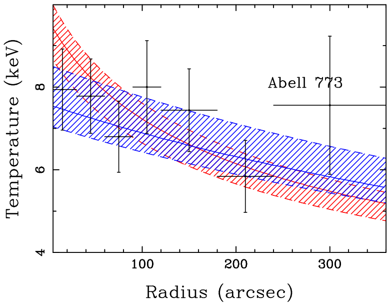
Abell 773
Temperature (keV)
4
6
8
100
200
300
Radius (arcsec)

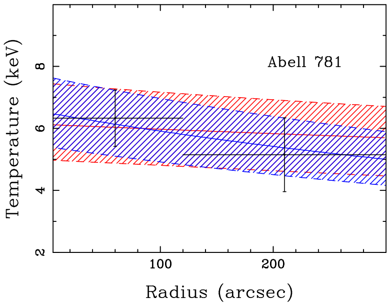
Abell 781
Temperature (keV)
2
4
6
8
100
200
Radius (arcsec)

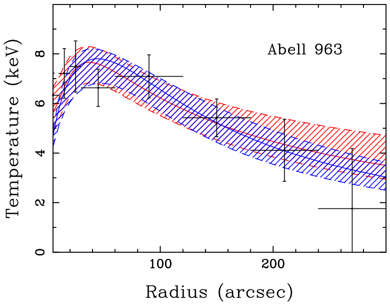
Abell 963
Temperature (keV)
0
2
4
6
8
100
200
Radius (arcsec)

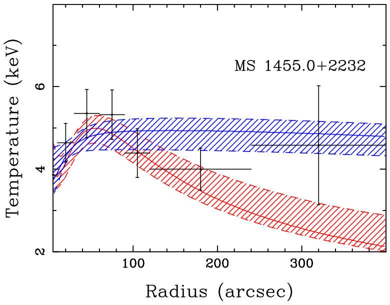
MS 1455.0+2232
Temperature (keV)
2
4
6
100
200
300
Radius (arcsec)

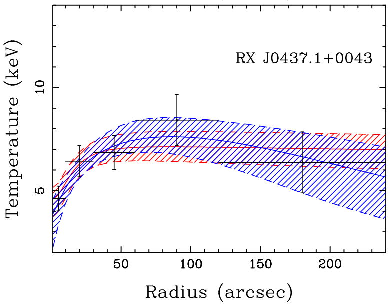
RX J0437.1+0043
Temperature (keV)
5
10
50
100
150
200
Radius (arcsec)

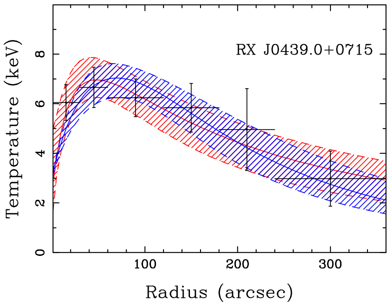
RX J0439.0+0715
Temperature (keV)
0
2
4
6
8
100
200
300
Radius (arcsec)

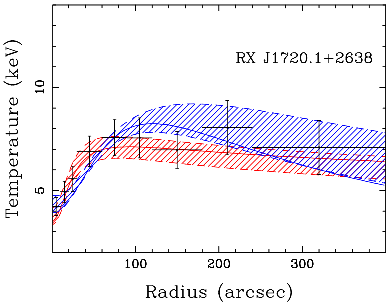
RX J1720.1+2638
Temperature (keV)
5
10
100
200
300
Radius (arcsec)

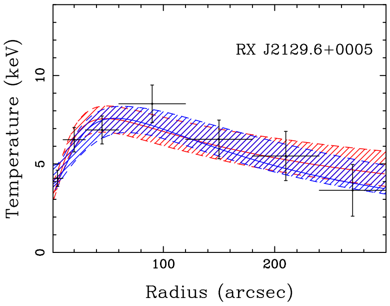
RX J2129.6+0005
Temperature (keV)
0
5
10
100
200
Radius (arcsec)

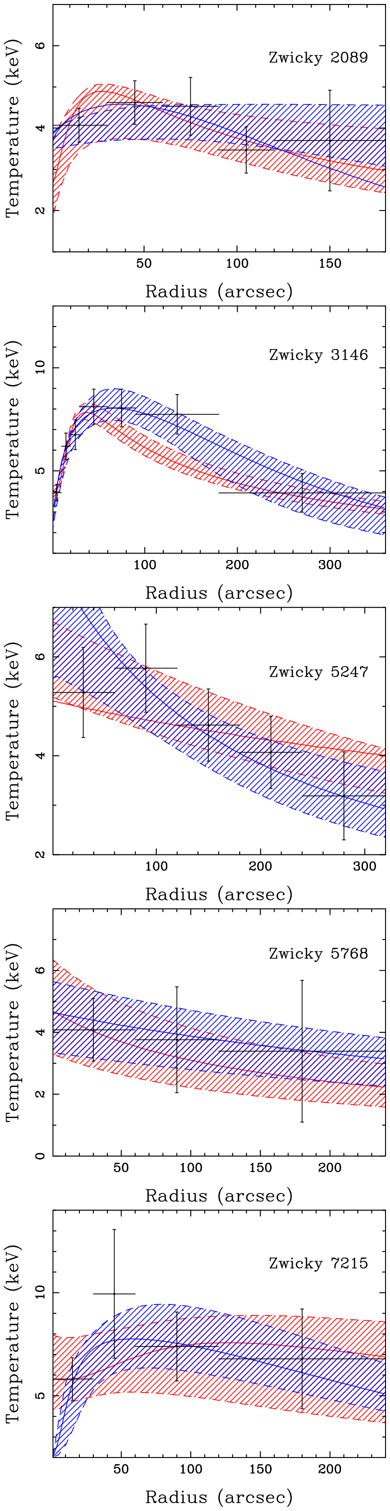

Figure 12. Temperature profiles for all clusters using the Vikhlinin et al. (2006) model (blue) and the Bulbul et al. (2010) model (red). The solid lines show the best-fit values, and the hatched region is the 68.3% confidence interval.